Monthly Notices of the ROYAL ASTRONOMICAL SOCIETY

MNRAS **537,** 3027–3052 (2025) https://doi.org/10.1093/mnras/staf208
Advance Access publication 2025 February 5

BOWIE-ALIGN: *JWST* reveals hints of planetesimal accretion and complex sulphur chemistry in the atmosphere of the misaligned hot Jupiter WASP-15b

James Kirk [1]★ Eva-Maria Ahrer [2] Alastair B. Claringbold [3,4] Maria Zamyatina [5] Chloe Fisher [6] Mason McCormack [7] Vatsal Panwar [3,4] Diana Powell [7] Jake Taylor [6] Daniel P. Thorngren [8] Duncan A. Christie [2] Emma Esparza-Borges [9,10] Shang-Min Tsai [11] Lili Alderson [12,13] Richard A. Booth [14] Charlotte Fairman [12] Mercedes López-Morales [15] N. J. Mayne [5] Annabella Meech [6,16] Paul Mollière [2] James E. Owen [1] Anna B.T. Penzlin [1] Denis E. Sergeev [5] Daniel Valentine [12] Hannah R. Wakeford [12] and Peter J. Wheatley [3,4]

Affiliations are listed at the end of the paper

Accepted 2025 January 29. Received 2025 January 29; in original form 2024 October 1

ABSTRACT

We present a transmission spectrum of the misaligned hot Jupiter WASP-15b from 2.8–5.2 microns observed with *JWST*'s NIRSpec/G395H grating. Our high signal-to-noise data, which has negligible red noise, reveals significant absorption by H_2O (4.2σ) and CO_2 (8.9σ). From independent data reduction and atmospheric retrieval approaches, we infer that WASP-15b's atmospheric metallicity is supersolar ($\gtrsim 15\times$ solar) and its carbon-to-oxygen ratio is consistent with solar, that together imply planetesimal accretion. Our general circulation model simulations for WASP-15b suggest that the carbon-to-oxygen ratio we measure at the limb is likely representative of the entire photosphere due to the mostly uniform spatial distribution of H_2O, CO_2, and CO. We additionally see evidence for absorption by SO_2 and absorption at 4.9 μm, for which the current leading candidate is OCS (carbonyl sulphide), albeit with several caveats. If confirmed, this would be the first detection of OCS in an exoplanet atmosphere and point towards complex photochemistry of sulphur-bearing species in the upper atmosphere. These are the first observations from the BOWIE-ALIGN survey which is using *JWST*'s NIRSpec/G395H instrument to compare the atmospheric compositions of aligned/low-obliquity and misaligned/high-obliquity hot Jupiters around F stars above the Kraft break. The goal of our survey is to determine whether the atmospheric composition differs across two populations of planets that have likely undergone different migration histories (disc versus disc-free) as evidenced by their obliquities (aligned versus misaligned).

Key words: methods: observational – exoplanets – planets and satellites: atmospheres.

1 INTRODUCTION

One of the main goals behind many exoplanet atmosphere observational programmes is to learn about exoplanet formation and evolution. A primary focus of the field has been to use a planet's carbon-to-oxygen ratio (C/O) to infer where a planet formed relative to ice lines in a protoplanetary disc, largely motivated by Öberg, Murray-Clay & Bergin (2011). However, there are many competing physical processes which make inferences from C/O challenging. These include the evolving ice lines within a disc (e.g. Morbidelli et al. 2016; Owen 2020), the drift of volatile-carrying solids in the disc (e.g. Booth et al. 2017; Schneider & Bitsch 2021), the relative importance of solid versus gaseous accretion in setting a planet's atmospheric composition (e.g. Espinoza et al. 2017), and the diversity found from observations of protoplanetary discs (e.g. Law et al. 2021). Furthermore, it is likely that observations of exoplanetary atmospheres probe a limited range of atmospheric pressures (Dobbs-Dixon & Cowan 2017), which might not be representative of the bulk planet's atmospheric composition due to processes such as local atmospheric mixing (e.g. Zamyatina et al. 2024), cloud formation (e.g. Helling et al. 2016), or a planet's interior evolution (Müller & Helled 2024). Therefore, it remains to be observationally demonstrated that C/O, and atmospheric composition in general, are reliable tracers of planet formation.

As Penzlin & Booth et al. 2024 showed, the high dimensionality and unconstrained nature of key planet formation and disc parameters make it challenging to predict the atmospheric composition of an exoplanet from planet formation models. However, they demonstrated that comparing populations of planets with different migration histories could constrain planet formation models. Specifically, they showed that the C/O and metallicity of exoplanets that migrate through a disc should diverge from exoplanets that undergo disc-free migration, due to the fact that disc-migrated planets accrete inner

★ E-mail: j.kirk22@imperial.ac.uk

disc material, a result that builds upon earlier work of Madhusudhan, Amin & Kennedy (2014) and Booth et al. (2017). However, the amplitude and sign of this divergence is dependent on whether silicates from the inner disc release their oxygen into the planetary atmosphere upon accretion and the uncertain form of the dominant carbon carriers in discs.

These theoretical considerations motivate our observational survey which seeks to compare the compositions of four aligned/low-obliquity hot Jupiters that likely migrated through their protoplanetary discs versus four misaligned/high-obliquity hot Jupiters that likely underwent disc-free migration via high-eccentricity migration (e.g. Rasio & Ford 1996; Wu & Murray 2003; Ford & Rasio 2008; Muñoz, Lai & Liu 2016). In our sample, we only include hot Jupiters orbiting F stars above the Kraft break (effective temperatures $\gtrsim 6100$ K) where tidal realignment is inefficient due to the stars' radiative envelopes (e.g. Albrecht et al. 2012). This reduces the likelihood of our aligned sample being polluted with initially misaligned planets that have had their obliquities damped. Kirk et al. (2024a) gives more detail regarding our survey ('BOWIE-ALIGN', Bristol, Oxford, Warwick, Imperial, Exeter - A spectral Light Investigation into hot gas Giant origiNs, *JWST* programme ID: GO 3838, PIs: Kirk & Ahrer). By comparing aligned versus misaligned hot Jupiters, our goals are to constrain planet formation models (e.g. Penzlin & Booth et al. 2024) and to robustly test the reliability of C/O and metallicity as tracers of planet formation.

In this work, we present the first observations from our programme, those of the hot Jupiter WASP-15b. WASP-15b, discovered by West et al. (2009), has a mass of $0.542^{+0.054}_{-0.053}$ M_J a radius of 1.428 ± 0.077 R_J (Bonomo et al. 2017), and an equilibrium temperature of 1676 ± 29 K (Southworth et al. 2013). Importantly for our programme, it has a precisely measured sky-projected obliquity ($\lambda = -139.6^{+4.3}_{-5.2}$; Triaud et al. 2010) and orbits an F7 dwarf star above the Kraft break (1.18 ± 0.12 $M_\odot$, 1.477 ± 0.072 $R_\odot$; Bonomo et al. 2017; $T_{\rm eff} = 6372 \pm 13$ K; Gaia Collaboration 2023). Our study is the first published transmission spectrum of WASP-15b.

We describe our observations in Section 2 and our data reduction in Section 3 that results in the planet's transmission spectrum (Section 3.3). In Section 4, we present constraints on the planet's atmospheric metallicity derived from interior structure models. We interpret the transmission spectrum using 1D atmospheric models in Section 5, a 3D general circulation model (GCM) in Section 6, and photochemical models in Section 7. We discuss our results in Section 8 and conclude in Section 9.

2 OBSERVATIONS

We observed one transit of WASP-15b on 2024 January 26, with the *JWST*/NIRSpec instrument (Jakobsen et al. 2022) in Bright Object Time Series mode. We used the G395H grating, *F290LP* filter, 2048 subarray and the NRSRAPID (NIRSpec rapid) read-out pattern. This set-up covers opacity from H_2O, CO_2, CO, and SO_2 (Alderson et al. 2023) between wavelengths of 2.8 and 5.2 μm at an average spectral resolution of $R = 2700$. We chose to use 44 groups per integration, which was informed by WASP-15's K magnitude of 9.7, and we acquired 685 integrations over 7.72 h, which included a baseline of 2.26 h pre-ingress and 1.65 h post-egress. Due to the brightness of WASP-15, we used a nearby, fainter star for target acquisition (2MASS J13554509−3209041[1]), observed with the SUB32 array and CLEAR filter.

[1]2MASS stands for Two Micron All Sky Survey (Skrutskie et al. 2006)

3 DATA REDUCTION

We performed three independent reductions of the data, one using the TIBERIUS pipeline (Kirk et al. 2017, 2021) and the other two using the EUREKA! pipeline (Bell et al. 2022). This approach was motivated by the work of the Early Release Science programme that demonstrated the benefits of independent data reductions (Ahrer et al. 2023; Alderson et al. 2023; Feinstein et al. 2023; JWST Transiting Exoplanet Community Early Release Science Team 2023; Rustamkulov et al. 2023). We give more information about our survey's data analysis strategy in Kirk et al. (2024a). We describe the approaches taken by the independent reductions for this work in the following sections.

3.1 TIBERIUS reduction

TIBERIUS (Kirk et al. 2017, 2021) is an open-source PYTHON-based code that has been used in several studies of *JWST* data from multiple instruments (e.g. Alderson et al. 2023; Rustamkulov et al. 2023; Kirk et al. 2024b).

3.1.1 Light curve extraction

We began by processing the raw images (`uncal.fits` files) through the standard set of Stage 1 steps[2] of the `jwst` pipeline (v1.8.2). However, we did not perform the `jump` step as it has been found to increase the noise in exoplanet transit light curves (e.g. Rustamkulov et al. 2023), and performed our own 1/f correction before the `ramp_fit` step. This involved subtracting the median value for each column on the detector after masking the 22 pixels centred on the stellar trace. The result of Stage 1 was the production of `gainscalestep.fits` files with flux units of DN/s. We additionally performed the `assign_wcs` and `extract_2d` steps of the `jwst` pipeline to obtain the wavelength solution.

Next, we performed our own cosmic ray/bad pixel identification and removal. First, we calculated the running median for every pixel's time series with a sliding box of three pixels and subtracted this running median from every pixel's time series. We then used the residuals to identify 5σ outliers and replaced these outliers with the running median's value. We chose a sliding box of 3 pixels to locate sharply varying features and to allow the pixel replacement to be informed by the neighbouring values in the time series. We also generated our own bad pixel mask at this stage. To do this, we combined the pixels flagged during Stage 1 as bad, saturated, dead or hot with pixels identified as 5σ outliers in a median-combined science integration from the first segment of data (260 integrations).

For each outlier-clipped integration, we then located the stellar trace by fitting a Gaussian to each row in the cross-dispersion direction, followed by a smoothing with a fourth-order polynomial. We then performed standard aperture photometry with an aperture full width of 8 pixels, after subtracting the background flux which was calculated as the median of the 10 pixels after masking 22 pixels centred on the trace. This aperture width was selected because of the lower noise in the resulting white light curves as compared to aperture widths of 6 and 10 pixels. We extracted the stellar flux between pixel rows 608 and 2044 (zero-indexed) for the NIRSpec 1 detector (NRS1) and between rows 3 and 2043 for the NIRSpec 2 detector (NRS2). With the stellar spectra in hand, we proceeded to create

[2]https://jwst-pipeline.readthedocs.io/en/latest/jwst/pipeline/calwebb_detector1.html#calwebb-detector1

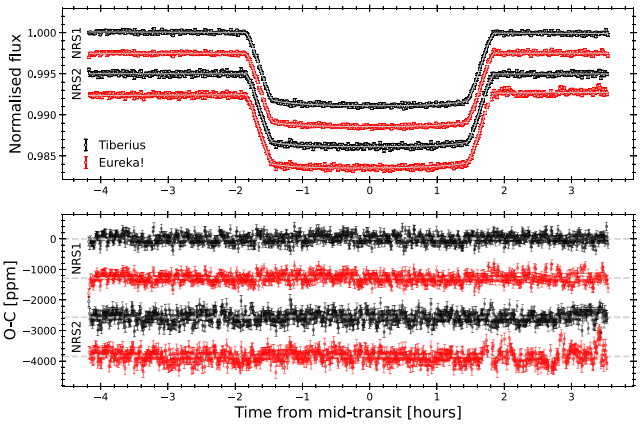

Figure 1. The white light curves and fits from two independent reductions. Top panel: the white light curves from TIBERIUS (black) and EUREKA! (red). The thin grey lines indicate the best-fitting models. The light curves from NRS1 and NRS2 are offset from one another for visualization. Bottom panel: the residuals from the fits in the top panel.

our light curves. For the white light curves, we integrated between wavelengths of 2.75 and 3.72 μm for the NRS1 detector and between 3.82 and 5.18 μm for the NRS2 detector. For our spectroscopic light curves, we adopted three different binning schemes: $R = 100$ (~ 61 pixels wide), $R = 400$ (~ 15 pixels wide), and 1 pixel resolution. Here, we present results from the $R = 100$ and $R = 400$ analyses, with the high resolution (1 pixel) analysis presented in a follow-up study (Esparza-Borges et al., in preparation).

3.1.2 Light curve fitting

We fit the NRS1 and NRS2 white light curves independently to obtain our own set of system parameters, using a `batman` (Kreidberg 2015) analytic transit light curve model multiplied by a linear-in-time polynomial. The free parameters in our white light curve fits were: the time of mid-transit (T_0), the planet's inclination (i), the planet's semimajor axis relative to the stellar radius (a/R_*), the relative planet-to-star radii (R_P/R_*), and the two coefficients of the linear polynomial. We held the orbital period fixed to 3.7520998 d (Patel & Espinoza 2022) and the planet's eccentricity to 0 (West et al. 2009). We used a quadratic limb darkening law and fixed the coefficients to the values computed by `ExoTiC-LD` (Grant & Wakeford 2024) using the `Stagger` grid of 3D stellar atmosphere models (Magic et al. 2015) and the stellar parameters from Bonomo et al. (2017) ($\log g = 4.17$ cgs, [Fe/H] $= -0.17$) and Gaia Collaboration (2023) ($T_{\rm eff} = 6372$ K).

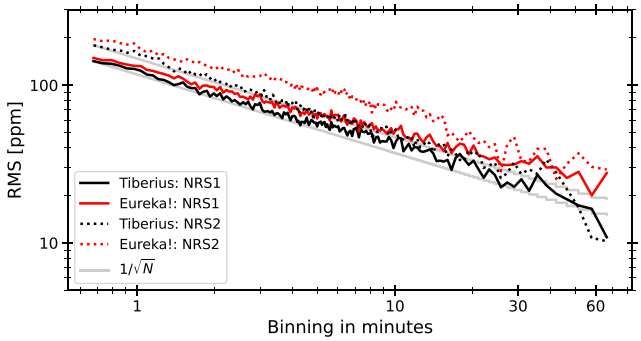

Figure 2. The Allan variance plot from the TIBERIUS (black) and EUREKA! (red) white light curve fits. The results for NRS1 are shown by the solid lines and NRS2 by the dotted lines. These closely follow the expectations from pure white noise (grey lines) which indicates a lack of red noise in the residuals.

We used a Levenberg–Marquadt algorithm, implemented through SCIPY (Virtanen et al. 2020), to explore the parameter space and determine the best-fitting parameters. For each light curve, we ran two sets of fits. The first fit allowed us to rescale the photometric uncertainties to give $\chi^2_\nu = 1$ for the best-fitting model. The second fit was performed with the rescaled uncertainties. The results from this second fit were used in the rest of our analysis.

The results from our white light curve fits are shown in Fig. 1 and Table 1. The system parameters from both detectors are consistent with one another and with values from the Transiting Exoplanet Survey Satellite,*TESS*, (Patel & Espinoza 2022). As shown by the Allan variance plots in Fig. 2, the residuals from the white light curve fits show minimal red noise. This is likely due to a combination of the relatively high groups/integration of our observations (44), the choice to fill 80 per cent of the full well and the relatively quiet nature of this F-type star. The Allan variance plots for the spectroscopic light curves are given in Appendix A and show that there is also minimal red noise in the spectroscopic light curves.

After the white light curve fits, we fit the spectroscopic light curves following the same procedure but with a/R_*, i, and T_0 fixed to the weighted mean values in Table 1. The spectroscopic light curves, models and residuals are shown in Fig. 3.

3.2 EUREKA! reduction

We utilized the open-source pipeline EUREKA! (v0.11.dev245+ge8ea1d1c.d20240701; Bell et al. 2022) to reduce our data for two additional analyses. EUREKA! has been successfully applied to *JWST* data sets and benchmarked against other pipelines (e.g. Ahrer et al.

Table 1. The resulting system parameters from our fits to the *JWST* NIRSpec/G395H white light curves. We include the values from the *TESS* analysis of Patel & Espinoza (2022) for comparison. The *TESS*T_0 has been propagated to the *JWST* transit epoch and accounts for the uncertainties in T_0 and P from Patel & Espinoza (2022).

Pipeline	Instrument	T_0 (BJD)	R_P/R_*	a/R_*	i (°)
TIBERIUS	NRS1	$2460336.666378 \pm 0.000035$	0.092858 ± 0.000068	7.524 ± 0.033	86.160 ± 0.068
TIBERIUS	NRS2	$2460336.666412 \pm 0.000043$	0.092961 ± 0.000084	7.535 ± 0.042	86.184 ± 0.085
TIBERIUS	Weighted mean	$2460336.666392 \pm 0.000027$	0.092899 ± 0.000053	7.528 ± 0.026	86.167 ± 0.053
EUREKA!	NRS1	$2460336.666404 \pm 0.000038$	0.093377 ± 0.000089	7.522 ± 0.064	86.130 ± 0.065
EUREKA!	NRS2	$2460336.666484 \pm 0.000053$	0.093759 ± 0.000098	$7.545^{+0.035}_{-0.037}$	$86.217^{+0.070}_{-0.074}$
EUREKA!	Weighted mean	$2460336.666441 \pm 0.000033$	0.093577 ± 0.000070	$7.536^{+0.023}_{-0.024}$	$86.177^{+0.047}_{-0.050}$
Patel & Espinoza (2022)	*TESS*	$2460336.667068 \pm 0.004240$	$0.0938^{+0.0009}_{-0.0012}$	$7.59^{+0.33}_{-0.28}$	$86.22^{+0.44}_{-0.63}$

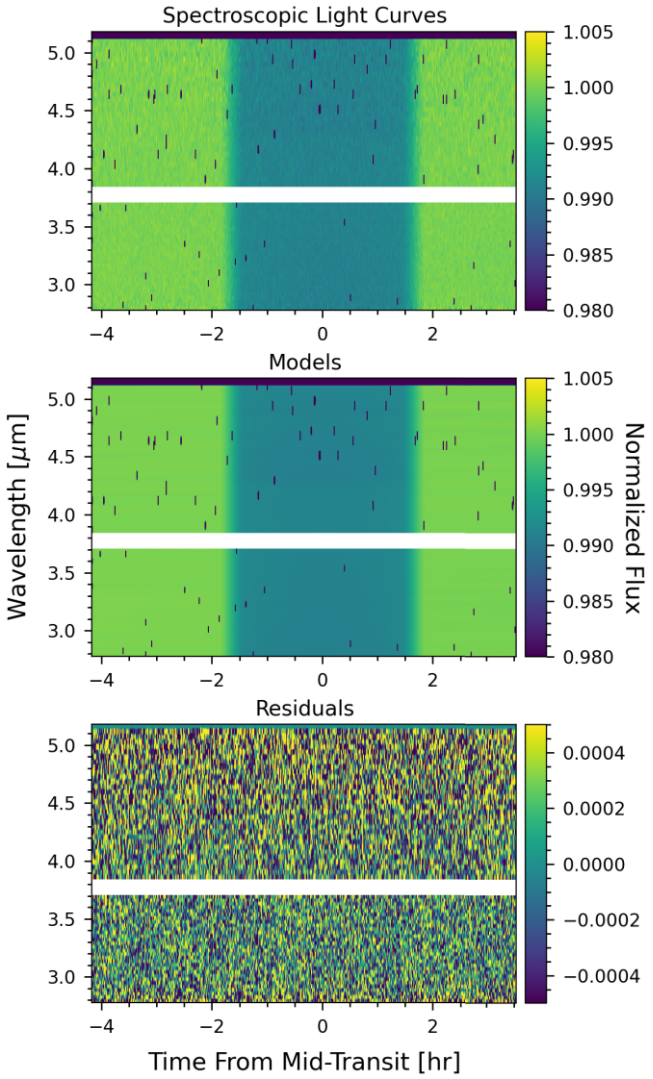

Figure 3. The $R = 100$ spectroscopic light curves and fits from the TIBERIUS reduction. The horizontal white bars correspond to the wavelengths of the gap between the detectors. Top panel: the spectroscopic light curves for NRS1 and NRS2. Middle panel: the best-fitting light curve models. Bottom panel: the residuals from the light curve fits.

2023; Moran et al. 2023). We describe the principal EUREKA! reduction in the following section. The second EUREKA! reduction was done independently with a different choice of reduction parameters and is presented in Appendix B.

3.2.1 Light curve extraction

We started our analysis with the raw images (`uncal.fits` files) and ran Stages 1 and 2 of EUREKA!, which are wrapped around the default `jwst` pipeline (v1.12.2) steps. We followed the default steps similar to the TIBERIUS but including the `jump` step with a threshold of 10σ which is larger than the `jwst` pipeline default value. We used the additional 1/f background subtraction at the group-level using the routine in EUREKA! before the ramp fit and we opted to use a custom scale factor (using a smoothing filter calculated from the first group) for the bias correction. We performed this step because it has been found to minimize transit depth offsets between the NRS1 and NRS2 detectors in other data sets (Moran et al. 2023).

EUREKA!'s Stage 3 performs the spectral extraction of the data. First, we rejected outliers > 3 times the median absolute deviation in the spatial direction and performed double-iterative masking of $> 5\sigma$ outliers along the time axis. We also masked bad pixels flagged by the `jwst` pipeline's data quality (`dq_init`) step. This is followed by a correction for the curvature of the spectral trace and a median-subtraction of the background for each frame using the area > 8 pixels away from the central pixel of the spectral trace (i.e. masking the trace with a full width of 17 pixels). Then we used a full width of 9 pixels for the optimal spectral extraction.

The extracted spectra were generated and binned in Stage 4, where we clipped $> 5\sigma$ outliers from both NRS1 and NRS2 based on a rolling median of 5 pixels.

We followed the same binning schemes as in the TIBERIUS pipeline, i.e. we computed a broad-band (white) light curve, as well as $R = 100$, $R = 400$, and pixel-level light curves. At this point we also generated limb-darkening coefficients using the same approach as in the TIBERIUS reduction.

3.2.2 Light curve fitting

In EUREKA!'s Stage 5 we fit our extracted light curves using a `batman` transit light curve model (Kreidberg 2015) and a linear-in-time polynomial. We used the Markov chain Monte Carlo (MCMC) sampling algorithm EMCEE (Foreman-Mackey et al. 2013) where the starting parameter values were set to the results of an initial least-squares fit.

Similarly to the TIBERIUS reduction, we fit the NRS1 and NRS2 white light curves independently and retrieved the system parameters a/R_*, inclination and mid-transit time. Like TIBERIUS, we held the period fixed to 3.7520998 d (Patel & Espinoza 2022) and assumed a circular orbit. We used the quadratic limb-darkening law, with the first coefficient, $u1$, fixed to the values obtained by `ExoTiC-LD` (Grant & Wakeford 2024) using the same stellar parameters as used by TIBERIUS (Section 3.1) and the same 3D `Stagger` models (Magic et al. 2015). However, unlike the TIBERIUS reduction, we fitted the second coefficient, $u2$, as a free parameter in all light curve fits. The retrieved system parameters for NRS1 and NRS2 were fixed when fitting the spectroscopic light curves for the respective detectors. These system parameters are given in Table 1. The white light curves and best-fitting models are shown in Fig. 1. The Allan variance plots from the white light curve fits are shown in Fig. 2 and the spectroscopic light curves in Fig. A1.

3.3 The transmission spectrum of WASP-15b

Fig. 4 shows WASP-15b's transmission spectrum at $R = 100$ and $R = 400$ from TIBERIUS and EUREKA!. There are two things to note from this comparison. First, there is a median transit depth offset between the two pipelines' spectra of 38 ppm, which is 70 per cent of the median 1σ transit depth uncertainty of 55 ppm. Secondly, there is a slope difference between the NRS2 spectra. We discuss the possible causes of these differences in Section 8.1.1. Looking beyond the comparison between the pipelines, the spectra reveal significant absorption features, which we explore in Sections 5 and 6.

4 CONSTRAINTS FROM INTERIOR STRUCTURE MODELS

Before we infer WASP-15b's atmospheric metallicity from its transmission spectrum, we investigated plausible metallicities for this planet using the interior structure models of Thorngren &

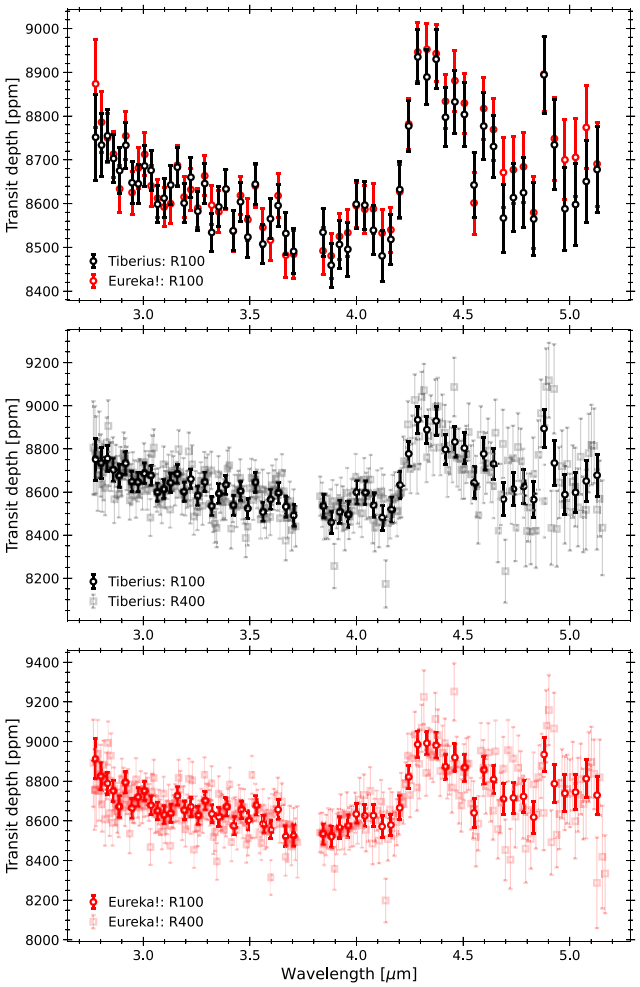

Figure 4. WASP-15b's transmission spectrum. Top panel: the comparison between the spectra obtained with TIBERIUS (black) and EUREKA! (red) at $R = 100$. The EUREKA! spectrum has been offset by -38 ppm to match the median transit depth of TIBERIUS. Middle panel: the spectrum at $R = 100$ (black) and $R = 400$ (grey squares), both obtained with TIBERIUS. Bottom panel: the spectrum at $R = 100$ (red) and $R = 400$ (light red squares), both obtained with EUREKA!.

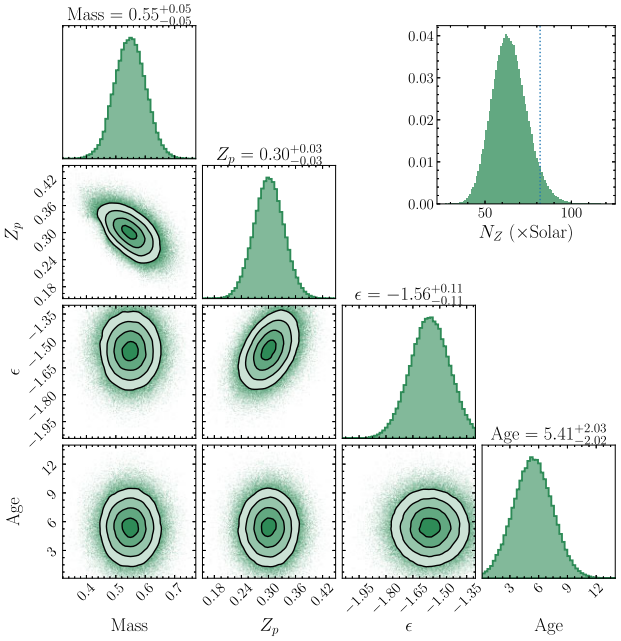

Figure 5. The posterior of the parameters of our interior structure model of WASP-15b: mass (M_J), Z_p (unitless mass ratio), ϵ (unitless heating power parameter), and the age (Gyr). The interior and statistical models used are identical to that of Thorngren & Fortney (2019). We find that the planet is moderately metal-rich with $Z_p = 0.30 \pm 0.03$, corresponding to a 95 per cent upper limit on the atmospheric composition of 82× solar.

Fortney (2019). These models solve the 1D structure equations for giant planets, with the hot Jupiter heating power set according to Thorngren & Fortney (2018), and a metallicity prior set according to the mass–metallicity relation of Thorngren et al. (2016). In order to set an upper limit on the potential atmospheric metallicity, these models assume a fully mixed interior – no core to hide additional bulk metal.

We fit the models using the same Bayesian framework as Thorngren & Fortney (2019). For the planet's mass, we adopted the value from Bonomo et al. (2017) of $0.542 \pm 0.054\,M_J$. For the age, we used a value of 5.40 ± 2.05 Gyr which we estimate as the median of Bonomo et al. (2017)'s asymmetric age distribution ($3.9^{+2.8}_{-1.3}$ Gyr). However, at these mature ages and for hot Jupiters in particular, the choice of age has little effect on the inferred bulk metallicity. For the planet's radius and flux/irradiation, we use values derived from our *JWST* data ($1.335 \pm 0.065\,R_J$ and $1.65\,\mathrm{Gerg\,s^{-1}\,cm^{-2}}$, respectively[3]). This method leads us to infer that the bulk metallicity is $Z_p = 0.30 \pm 0.03$ in mass ratio (Fig. 5). Note that this is the statistical uncertainty and does not account for theoretical uncertainties in for example the equations of state used. Still, it serves as a useful upper limit when converted from mass ratio to number ratio in × solar units. Here, we take the solar ratio of Z:H to be 0.00104 (Asplund et al. 2009), though note that other authors choose 0.00208 (solar composition gas under planetary conditions); it is important for consistency to be clear which definition is used. We find that the 95th percentile of the metallicity distribution is 82× solar, corresponding to a mean molecular weight $\mu = 3.4$ amu, which we adopt as an upper limit on plausible atmospheric metallicities.

5 INTERPRETING THE SPECTRUM WITH 1D MODELS

In this section, we describe the inferences we make from interpreting the spectrum with 1D atmospheric forward models and retrievals. We describe the results from three independent approaches in this Section and compare these in the Discussion (Section 8.1.2).

5.1 PETITRADTRANS forward models

We implement a 1D forward model grid of synthetic transmission spectra using the PETITRADTRANS package (v2.7.7, Mollière et al. 2019; Nasedkin, Mollière & Blain 2024).

[3]The planet's radius was derived from our TIBERIUS R_P/R_*, and Bonomo et al. (2017)'s R_*. The flux was derived from Gaia DR3's $T_{\rm eff}$ (Gaia Collaboration 2016), our TIBERIUS a/R_* and Bonomo et al. (2017)'s R_*.

In both our forward models and retrievals with PETITRADTRANS (Section 5.2), we use correlated-k radiative transfer with opacity tables at $R = 1000$ to calculate the transmission spectra. The opacity tables were pre-computed from spectral lines, using the following line-lists from HITEMP: H_2O and CO (Rothman et al. 2010); and ExoMol: CO_2 (Yurchenko et al. 2020), SO_2 (Underwood et al. 2016), CH_4 (Yurchenko et al. 2017), H_2S (Azzam et al. 2016), OCS (Owens, Yurchenko & Tennyson 2024), HCN (Barber et al. 2014), C_2H_2 (Chubb et al. 2021), SO (Brady et al. 2024), and NH_3 (Coles, Yurchenko & Tennyson 2019). We assume a H_2- and He-dominated atmosphere and include opacity from $H_2 - H_2$ and H_2 – He collision-induced absorption as well as Rayleigh scattering from H_2 and He.

We use an initial grid of equilibrium chemistry simulations, with an isothermal temperature profile and the radius, mass, and equilibrium temperature of WASP-15b reported in Section 1, varying the C/O ratio from 0.1 to 1.0 and the metallicity from 0.1 to 100× solar. The equilibrium chemical composition is interpolated from a large grid pre-calculated using `easyCHEM`, as described in Mollière et al. (2017). We use the parametrization described in Mollière et al. (2015) using metallicity [Fe/H] and C/O ratio. The abundance of all atoms, including the C/H ratio, is scaled by metallicity relative to solar (as defined in Asplund et al. 2009), except the O/H ratio, which is further scaled by the C/O ratio relative to the C/H ratio.

Comparing this forward model grid by eye to both the TIBERIUS and EUREKA!$R = 100$ spectra revealed that a supersolar metallicity of 10–100× solar (Asplund et al. 2009), and a C/O ratio from 0.2 to 0.8 was required to give a similar spectrum, as seen in Fig. 6 (top panel). Leaving out opacity from one molecule at a time from the model revealed H_2O and CO_2 as the primary opacity sources, with potential minor contributions from CO and H_2S. None of these clear atmosphere simulations were simultaneously able to predict the strength of the main H_2O and CO_2 features, with $< 80\times$ solar metallicity models overpredicting the strength of the H_2O feature, and $> 50\times$ solar metallicity models underpredicting the strength of the CO_2 feature. We therefore extended our grid with simulations with a grey cloud deck at 0.1 mbar, a grey cloud deck at 10 mbar, or a cooler 1000 K isothermal atmosphere. We found that 0.1 mbar clouds, a cooler terminator temperature, or some combination thereof create a good fit to both features, as portrayed in Fig. 6 (bottom panel).

We were unable to generate satisfactory fits to the apparent features at 4.0 and 4.9 μm using equilibrium chemistry models. Motivated by the detection of SO_2 at 4.0 μm in the transmission of WASP-39b (Tsai et al. 2023), we tested this scenario for WASP-15b and found that the inclusion of a modest 5 ppm abundance of SO_2 can fit the feature (purple dashed line, Fig. 6, bottom panel), as described in Section 5.2. We tested a wide variety of molecules to explain the feature at 4.9 μm. We found that both OCS and O_3 had absorption centred at the right wavelengths but were generally broader than the feature width. We discuss the interpretation of this feature in more detail in Section 8.3. Using the TRIARC package (Claringbold et al. 2023), we found that, given the equilibrium chemistry forward model and precision of the observation, the abundances of SO_2 and OCS would need to be ≥ 10 and 1 ppm to constitute 3σ detections.

5.2 PETITRADTRANS retrievals

For a more detailed exploration of our transmission spectrum, we performed free chemistry and equilibrium chemistry retrievals on the $R = 100$ spectra from both TIBERIUS and EUREKA!. PETITRADTRANS uses Bayesian nested-sampling (Skilling 2004) implemented through

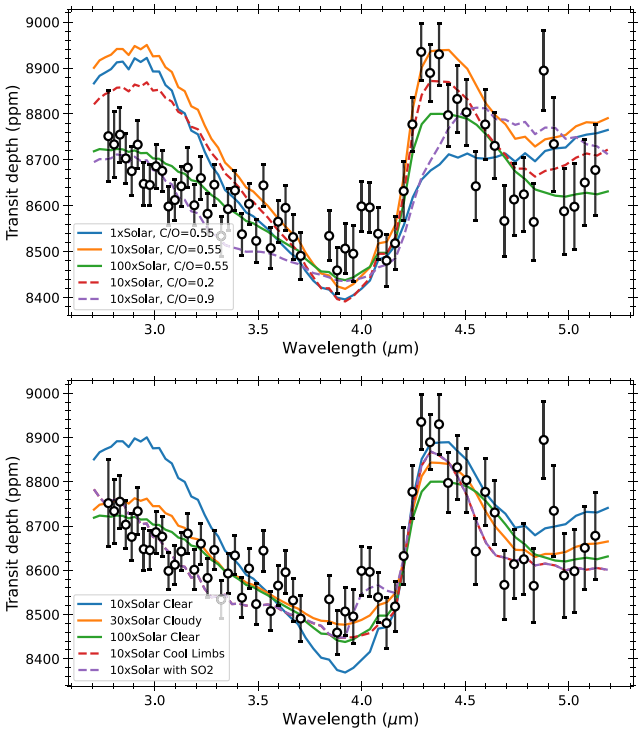

Figure 6. Top panel: selected synthetic transmission spectra from our PETITRADTRANS 1D equilibrium chemistry forward model grid, plotted against our TIBERIUS $R = 100$ spectrum of WASP-15b. The temperature profile is fixed to an isotherm at $T_{eq} = 1676$ K. We find that a ∼solar C/O ratio, and a metallicity $> 10\times$ solar is required to give the appropriate feature shapes, identifiable as H_2O and CO_2, but we are not able to match the feature amplitudes with this simple model. Bottom panel: selected synthetic transmission spectra from our expanded PETITRADTRANS 1D equilibrium chemistry forward model grid. This demonstrates that the inclusion of higher altitude clouds at 0.1 mbar (the cloudy model, orange) or fixing the isothermal temperature to a cooler value of 1000 K (the cool limbs model, green), combined with a 10–50× solar metallicity and C/O = 0.55 allows us to more successfully fit the feature amplitude compared to the original grid with no clouds and equilibrium temperature limbs (top panel). We additionally include a model with 5 ppm of SO_2 (purple dashed line, bottom panel).

MULTINEST (Feroz & Hobson 2008) with PYMULTINEST(Buchner et al. 2014). We used the same correlated-k opacities and isothermal temperature structure as the forward models of Section 5.1. We also included a grey cloud deck, with the cloud-top pressure as a free parameter, with a log uniform prior from 1 μbar to 100 bar. We used a Gaussian prior for the planet's gravity based on Bonomo et al. (2017), and wide, uniform priors for the planet's radius (0.8–1.8 R_J) and limb temperature (500–3000 K). The stellar radius was fixed to 1.477 $R_\odot$. We experimented with fitting the reference pressure at fixed planetary radius, to determine that a reference pressure of 1 mbar, at which the radius and gravity were defined, was most appropriate. We used a wide prior on the planet's radius because of our decision to fix the reference pressure in our retrieval; as the true reference pressure is unknown, we cannot use our prior knowledge of the radius in the retrieval without potentially biasing it. This is the most common approach for atmospheric retrievals (e.g. Alderson, Grant & Wakeford 2022; Taylor et al. 2023; Banerjee et al. 2024). We also ran a retrieval with a tight radius prior based on the white-light transit depth and a uniform reference pressure prior and found that it did not affect our results.

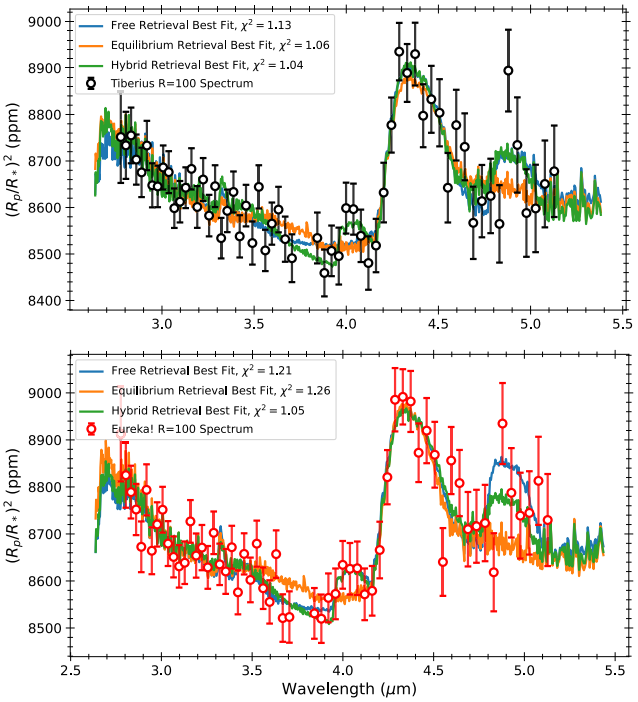

Figure 7. Best-fitting models from our PETITRADTRANS free chemistry (blue), equilibrium chemistry (orange), and hybrid chemistry (equilibrium chemistry plus free S-bearing species, green) retrievals, fitted to the TIBERIUS $R = 100$ reduction (top panel) and EUREKA! $R = 100$ reduction (bottom panel).

For our free chemistry retrievals, we permitted the log volume mixing ratio to vary from -12 to -0.5 for each molecule. For our chemical equilibrium retrievals, the elemental ratios were parametrized by C/O ratio and metallicity, as previously described. We used a uniform prior of 0.1 to 1.5 for C/O, and a log uniform prior of -2 to 3 on metallicity. Given the strong impact of photochemistry on sulphur species, which is not accounted for by chemical equilibrium, we also ran a hybrid retrieval where the H_2O, CH_4, CO, and CO_2 abundances are determined by chemical equilibrium, while the photochemically active sulphur species H_2S, SO_2, and OCS abundances are free parameters.

For each pair of retrievals, we found complete consistency in the retrieved parameters between the TIBERIUS and EUREKA! spectra. The complete retrieval results are summarized in Table E1. The best-fit models from each retrieval setup are shown in Fig. 7.

Our equilibrium chemistry retrievals infer a C/O ratio of $0.48^{+0.11}_{-0.16}$ for the TIBERIUS spectrum and $0.53^{+0.09}_{-0.16}$ for the EUREKA! spectrum, consistent with the solar value of 0.55 (using the solar metallicity of Asplund et al. 2009). The metallicity was determined to be supersolar, at $18^{+22}_{-8}\times$ solar and $22^{+27}_{-9}\times$ solar, respectively. We also retrieved a limb temperature of ~ 900 K, much colder than the equilibrium temperature, and minimal constraints on the cloud-top pressure, with a 3σ lower limit of 0.1 mbar.

Our free chemistry retrievals yielded similar results, ruling out H_2O and CO_2 abundances of less than 1 ppm. The log vertical mixing ratios were found to be $-2.83^{+0.59}_{-0.95}$ for H_2O and $-4.40^{+0.73}_{-1.02}$ for CO_2 in the TIBERIUS spectrum, with similar results for the EUREKA! spectrum. There were no firm constraints for other species in the TIBERIUS spectrum, but the posterior corner plot from the EUREKA! spectrum (see Fig. E1) indicates that one of CO or OCS is likely present in the spectrum (the posteriors are inconsistent with neither being present to 3σ), but they cannot be distinguished. Our free chemistry retrievals favoured a cloudy atmosphere, placing a maximum cloud-top pressure of ~ 0.1 bar.

Our hybrid retrievals provided the best-fit to the data, with reduced $\chi^2_\nu = 1.04$ for TIBERIUS and $\chi^2_\nu = 1.05$ for EUREKA!, as depicted in Fig. 7. By treating the sulphur species as free parameters, we could fit the features at 4.0 and 4.9 μm with SO_2 and OCS, respectively, while also permitting H_2S to be depleted due to photochemical destruction or a low S/H ratio, impacting the spectrum either side of the detector gap. This approach resulted in more precise constraints on the C/O ratio, with a retrieved C/O ratio of $0.53^{+0.09}_{-0.15}$ for the TIBERIUS spectrum and $0.56^{+0.07}_{-0.13}$ for the EUREKA! spectrum. The corner plot for the hydrid retrieval is shown in Fig. 8.

We also ran additional retrievals for the purpose of model comparison. By running additional free chemistry retrievals omitting a single species on the TIBERIUS $R = 100$ spectrum and comparing the Bayesian evidence (Trotta 2008; Benneke & Seager 2013), we were able to place the detection significance of CO_2 at 8.9σ, and H_2O at 4.2σ. We also repeated the hybrid chemistry retrievals, omitting in turn SO_2, OCS, and then both. We present a comparison of retrieval evidences in Table 2. In the EUREKA! spectrum, $\Delta \ln Z = +2.2$ between the equilibrium and hybrid retrievals, equivalent to a 2.6σ preference. This is the result of small improvements of evidence, none of which are individually significant, from including each of H_2S, SO_2, and OCS as free parameters. The TIBERIUS spectrum is agnostic between equilibrium and hybrid models, with a $\Delta \ln Z$ of only $+0.5$ between the best (hybrid with H_2S and OCS) and worst (hybrid with H_2S, SO_2, and OCS) models. We also included hybrid retrievals on the $R = 400$ spectra, to determine if the additional resolution could better resolve the SO_2 and OCS features. These results were completely consistent with the $R = 100$ retrievals, with the evidence marginally improving for each S-species added with the EUREKA! spectrum, but changing by less than 0.4 between different TIBERIUS set-ups.

5.3 BEAR retrieval

As a comparison, we also perform free-chemistry retrievals with the GPU-accelerated open-source BERN ATMOSPHERIC RETRIEVAL code (BEAR[4]). This is an updated version of the retrieval code previously known as HELIOS-R2 (Kitzmann et al. 2020). BEAR uses the MULTINEST library (Feroz & Hobson 2008) to perform the retrieval using Bayesian nested-sampling (Skilling 2004). It uses line-by-line opacity sampling, which we sampled at a resolution of 1.0 cm^{-1} in wavenumber (equivalent to $R \sim 2500$), and in this work we include the following molecules and their associated ExoMol line-lists: H_2O (Polyansky et al. 2018), CH_4 (Yurchenko et al. 2013), CO (Li et al. 2015), CO_2 (Yurchenko et al. 2020), SO_2 (Underwood et al. 2016), H_2S (Azzam et al. 2016), and OCS (Wilzewski et al. 2016). We also include opacity due to collision-induced absorption from H_2-H_2 (Abel et al. 2011) and H_2-He (Abel et al. 2012), as well as Rayleigh scattering from H_2 (Vardya 1962). We assume free-chemistry, for which the molecular abundances are allowed to vary from volume mixing ratios of 10^{-12} to 1.0. The rest of the atmosphere is composed of H_2 and He, assuming a solar ratio of 0.17 (Asplund et al. 2009). The atmosphere is divided into 200 equal layers in log-pressure space, assuming a top pressure of 10^{-8} bar, and a bottom pressure of 10 bar. We assume an isothermal temperature, sampled between 500

[4]BEAR can be found at https://github.com/newstrangeworlds/bear.

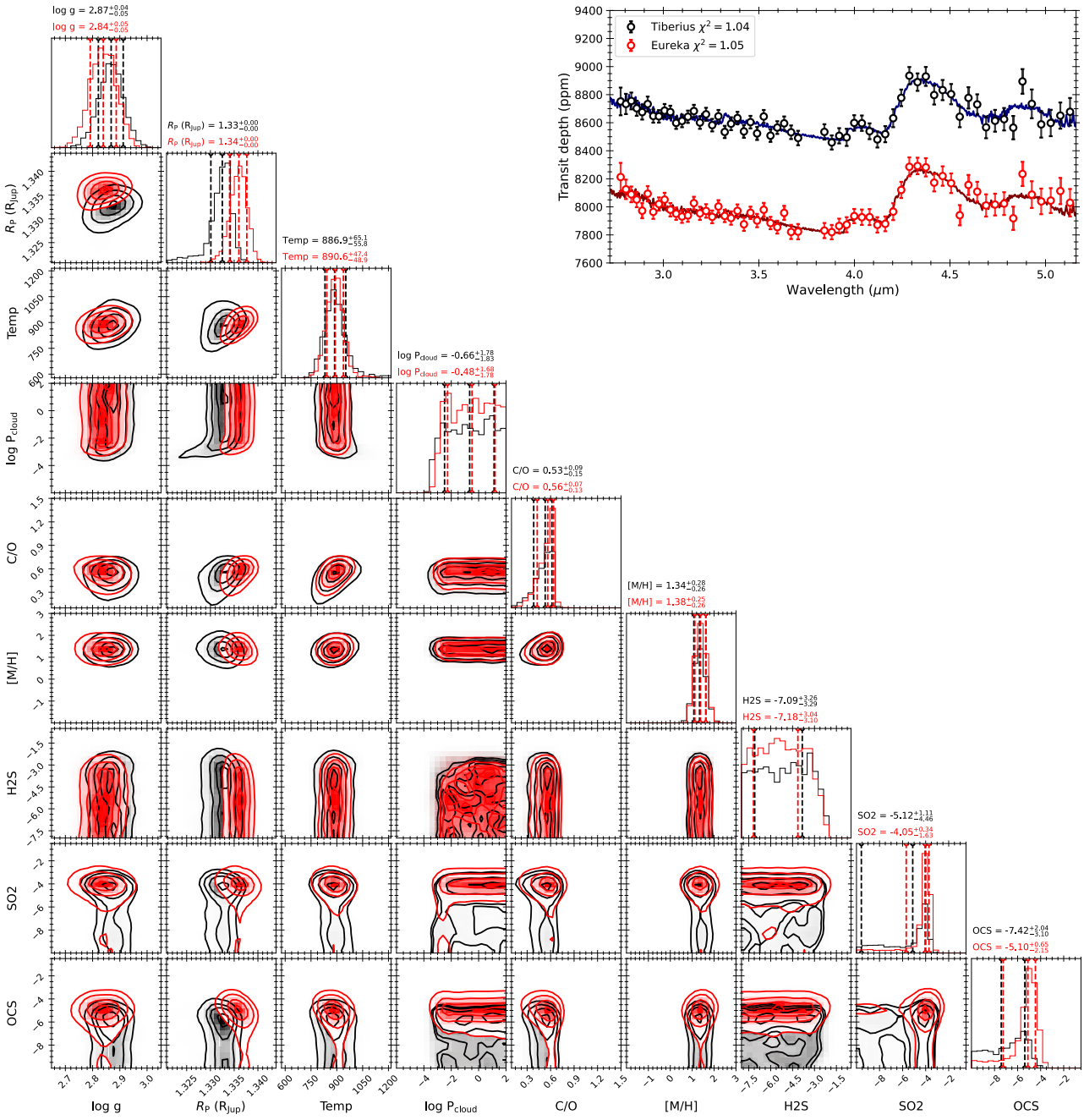

Figure 8. Corner plot showing the posterior PDFs from the hybrid PETITRADTRANS retrieval performed on the TIBERIUS $R = 100$ spectrum (black) and EUREKA! $R = 100$ spectrum (red). In the hybrid retrievals, the abundances of CH_4, CO_2, CO, and H_2O are fixed to their abundances at chemical equilibrium, while the abundances of S-bearing species H_2S, SO_2, and OCS are free parameters. The best-fitting model and residuals are displayed in the top right.

and 2500 K, and include a grey cloud deck, for which we retrieve a cloud-top pressure sampled between 10^{-5} and 10 bar. The stellar radius is fixed to 1.477 $R_\odot$, and the planet radius and gravity are free parameters. The planet radius uses a uniform prior of 1.27–1.40 R_J, and the gravity uses a Gaussian prior on log g with a mean of 2.828 and a standard deviation of 0.041, in cgs units. All BEAR retrievals in this work use 1000 live points.

We applied this retrieval code to both the TIBERIUS and EUREKA! reductions at $R = 100$ and $R = 400$. For the $R = 100$ case (shown in Fig. E2), we find a bimodal distribution for a number of parameters, representing two families of models. The first, favoured by the EUREKA! data, is composed of H_2O, CO, and CO_2, with a moderate water volume mixing ratio of $\sim 10^{-5}$. The second, favoured by the TIBERIUS data, only shows evidence for H_2O and CO_2, but now the water abundance is ~ 15 per cent. This corresponds to a very high-metallicity scenario, which is unphysical according to our interior structure model (see Section 4). For the $R = 400$ case, the retrieval favours the higher metallicity model in both reduction cases (not shown).

Motivated by the upper limits on WASP-15 b's atmospheric metallicity and mean molecular weight derived from our interior structure model, we recomputed our BEAR posteriors after excluding

Table 2. The Bayesian evidence ($\ln Z$) and degrees of freedom (DOF) from each of our PETITRADTRANS retrievals, including equilibrium chemistry, free chemistry, and hybrid retrievals with equilibrium CH_4, H_2O, CO, and CO_2 abundances, but the abundance of specified S-bearing species as free parameters. The evidence is very agnostic about the inclusion of various S-species in the TIBERIUS spectrum, but there is a moderate (2.6σ) preference for the hybrid chemistry model in the EUREKA! spectrum, implying some combination of H_2S depletion, OCS enrichment, and the presence of SO_2.

Retrieval	TIBERIUS $\ln Z$	EUREKA! $\ln Z$	DOF
Equilibrium	−40.0	−47.5	6
Hybrid (H_2S only)	−39.9	−46.3	7
Hybrid ($H_2S + SO_2$)	−40.0	−46.0	8
Hybrid (H_2S + OCS)	−39.8	−45.7	8
Hybrid (H_2S + OCS + SO_2)	−40.3	−45.3	9
Free	−43.0	−48.2	11

the high metallicity modes from our posteriors. Specifically, we summed the mass mixing ratios of the molecules and limited the metal-mass ratio to 0.36 (equal to the 2σ upper limit on Z_p, Section 4). The resulting posteriors are shown in Fig. 9. Now we see a good agreement between the EUREKA! and TIBERIUS retrievals, with a water volume mixing ratio of $\sim 10^{-6}$. In agreement with PETITRADTRANS, we retrieve limb temperatures of ∼900–1100 K. The cloud-top pressure is unconstrained in both reduction cases. The upper-right insert of Fig. 9 shows the best-fitting spectra for each of the retrievals, as well as the reduced χ^2 values for these fits.

5.4 PLATON retrieval

We also used the open source PLATON package (Zhang et al. 2019, 2020) to interpret our transmission spectra. PLATON assumes equilibrium chemistry in 1D and an isothermal pressure–temperature profile. In its default configuration, which we used here, PLATON includes opacities from 34 chemical species with equilibrium abundances calculated using `GGchem` (Woitke et al. 2018) over a large grid of metallicities, C/O, temperatures, and pressures. The full list of species, along with line lists, is given in Zhang et al. (2020). The dominant species at the wavelengths and temperatures we are concerned with here are: H_2O (Polyansky et al. 2018), CO_2 (Tashkun & Perevalov 2011), and CO (Faure et al. 2013; Gordon et al. 2017). PLATON also includes SO_2 (Underwood et al. 2016) by default but not OCS which, as we discuss in Section 8.3, may be responsible for the feature at 4.9 μm. For our analysis, we used the line lists generated at a spectral resolution of $R = 10000$ and the opacity sampling method of radiative transfer, rather than correlated-k.

In our PLATON retrievals we have five free parameters: the planet's radius (R_P), the temperature of the isothermal atmosphere (T_{iso}), the atmospheric metallicity ($\log Z$), the atmospheric C/O, and the pressure of a grey cloud deck ($\log P_{cloud}$). The metallicity is defined relative to solar (Asplund et al. 2009) and PLATON's default C/O ratio is 0.53. We place wide flat priors on each parameter of $1.20 < R_P < 1.47\,R_J$, $300 < T_{iso} < 2500\,K$, $-1 < \log Z < 3$, $0.05 < C/O < 2.0$, and $-1 < \log P_{cloud} < 5\,Pa$. We fixed the stellar radius to $1.477\,R_\odot$ and planet mass to $0.542\,M_J$ (Bonomo et al. 2017). We explored the parameter space using nested sampling, implemented through `DYNESTY` (Speagle 2020), with 1000 live points. We ran these retrievals for both the TIBERIUS and EUREKA! spectra at $R = 100$ and $R = 400$. The posterior medians, 16th and 84th percentiles are given for each fit parameter in Table E1 with the best-fitting models plotted in Fig. 10.

As shown in Table E1, our PLATON analysis favours supersolar metallicities of $> 29\times$ solar and $> 38\times$ solar to 1σ for TIBERIUS and EUREKA!, respectively. The median retrieved C/O for both reductions of the data are consistent with solar albeit with relatively large uncertainties ($C/O = 0.45^{+0.18}_{-0.20}$ and $0.54^{+0.15}_{-0.21}$ for TIBERIUS and EUREKA!, respectively). However, as we showed in Section 4, our interior structure models place a 2σ upper limit on WASP-15b's metal mass fraction of 0.36. If we exclude the retrieval samples with metal mass fractions greater than this and recalculate our posteriors, we find a revised metallicity constraint of 35^{+23}_{-19} and $41^{+21}_{-22}\times$ solar for TIBERIUS and EUREKA!, respectively, while C/O does not change significantly (Table E1). We consider these to be a more accurate inference of WASP-15b's true atmospheric metallicity. Fig. 10 shows the corner plot after excluding the unphysically high metallicity solutions. Fig. E3 shows the corner plot over the full metallitic range.

Table E1 demonstrates that our inferences with PLATON are insensitive to whether we run our retrievals on the $R = 100$ or $R = 400$ spectra. For this reason, we only plot the results from our $R = 100$ retrievals (Fig. 10).

In summary, all of our retrieval analyses converge to a supersolar metallicity with a C/O consistent with solar. For PLATON and BEAR, the loose metallicity prior allows for unphysically high metallicities which we exclude based on interior structure models of WASP-15b (Section 4). We discuss the comparison between the retrievals in more detail in Section 8.1.2.

6 INTERPRETING THE SPECTRUM WITH A 3D GENERAL CIRCULATION MODEL

To investigate the potential impact of spatial inhomogeneities in WASP-15b's atmosphere on the observed transmission spectrum, we performed simulations of WASP-15b's atmosphere using the `Met Office Unified Model` (`UM`), which is a 3D climate model of a planetary atmosphere (also known as a general circulation model, or a GCM). We used the same basic `UM` set-up as in Drummond et al. (2020) and Zamyatina et al. (2023, 2024) that provides the coupling between the dynamics, radiative transfer, and chemistry. In brief, `UM`'s dynamical core (`ENDGame`; Wood et al. 2014; Mayne et al. 2014a, b) solves the full, deep-atmosphere, non-hydrostatic equations of motion on a constant angular grid using a semi-implicit semi-Lagrangian scheme. The `UM`'s radiative transfer component (`SOCRATES`; Edwards 1996; Edwards & Slingo 1996; Amundsen et al. 2014, 2016, 2017) solves the two-stream equations and treats opacities using the correlated-k and equivalent extinction methods. Opacity sources considered in the radiative transfer include the absorption due to H_2O, CO, CO_2, CH_4, NH_3, HCN, Li, Na, K, Rb, Cs, and collision-induced absorption due to H_2-H_2 and H_2-He as well as Rayleigh scattering due to H_2 and He (for the line list information, see Goyal et al. 2020). Lastly, the `UM`'s chemistry component provides several chemical schemes for simulating the evolution of hot-Jupiter gas-phase chemistry, with the 'equilibrium' and 'kinetics' chemical schemes used in this study and described below. We chose a model grid resolution of 2.5° in longitude by 2° in latitude and 86 vertical levels equally spaced in height (covering pressures from ∼200 bar to $\sim 10^{-5}$ bar). This grid resolution is too coarse to resolve convection; however, we do not find that a convective adjustment or a similar correction is required. Even so, a longitudinal filter is used to maintain numerical stability, with the filtering constant of the horizontal wind, K, equal to 0.04 (see Mayne et al. 2014a, b; Christie et al. 2024). For the stellar spectrum we used a `PHOENIX` BT-Settl model (Rajpurohit et al. 2013) with

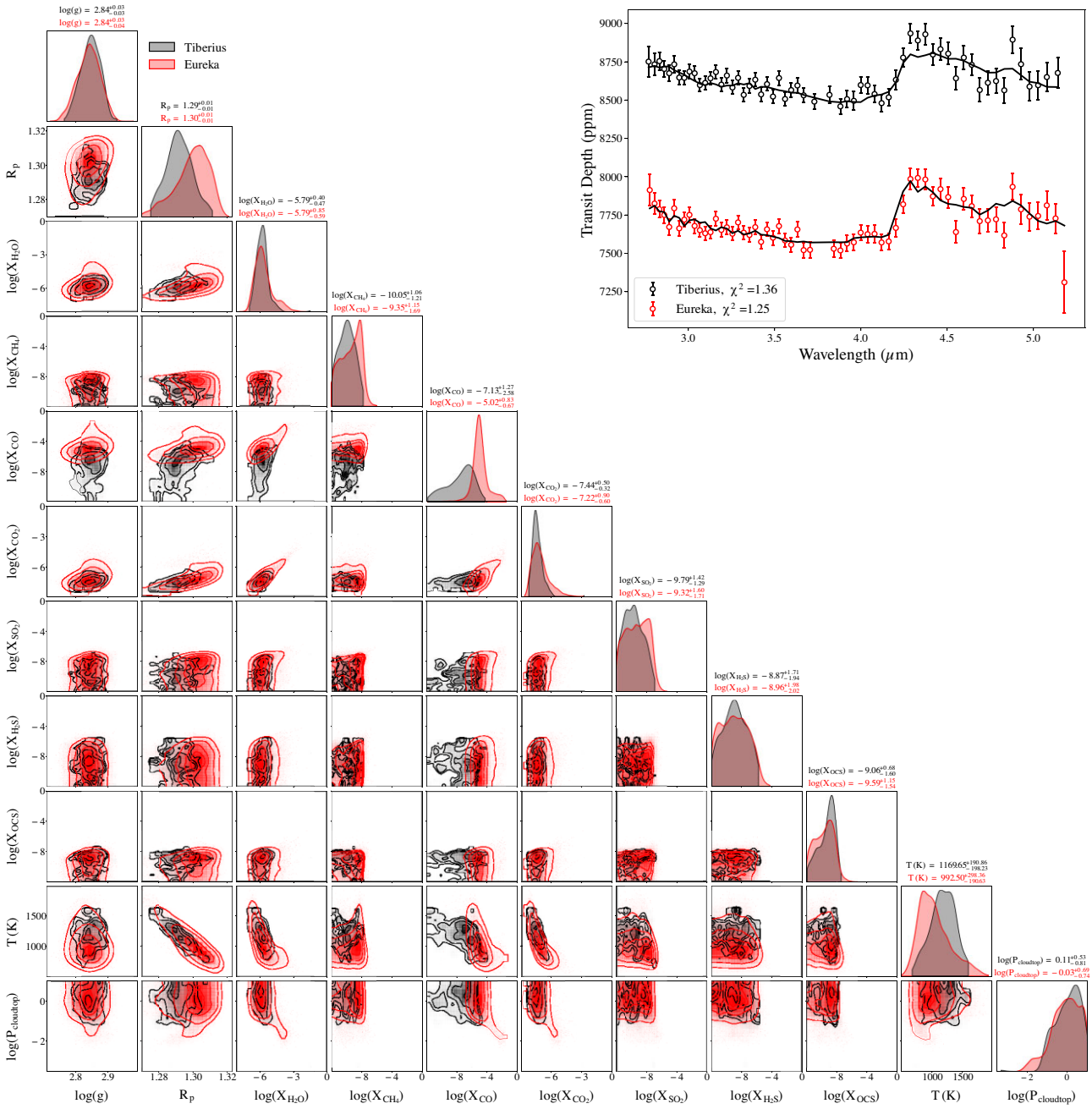

Figure 9. Corner plot showing the posteriors from the BEAR retrievals on the TIBERIUS (black) and EUREKA! (red) reductions of WASP-15 b at $R = 100$, restricted to the metallicities allowed by the interior structure model. The top right insert shows the best-fitting models for the TIBERIUS (black) and EUREKA! (red) reductions. The EUREKA! spectrum is offset by 1000 ppm for visualization purposes. The legend in the bottom left indicates the reduced χ^2 values for each of the fits.

parameters from Table F1, and for the planet – parameters from Table F2.

We performed two simulations. One simulation (which we refer to as the UM 'equilibrium' simulation), used a chemical equilibrium scheme to compute the change in chemical species abundances induced by the changes in atmospheric pressure and temperature only. The other simulation (which we refer to as the UM 'kinetics' simulation), allowed for departures from chemical equilibrium due to disequilibrium thermochemistry (but omitting photolysis) and used a kinetics chemical scheme to compute the change in chemical species abundances caused not only by the changes in atmospheric pressure and temperature, but also by the changes in the production and loss of these species during their atmospheric transport. Chemical species included in both UM simulations were those present in the Venot et al. (2019) C-O-N-H reduced chemical network. Abundances of alkali metals not included in the Venot et al. (2019) network – Li, Na, K, Rb, and Cs – were calculated using a threshold method outlined in Amundsen et al. (2016). Both UM simulations assumed an aerosol-free atmosphere with 10× solar metallicity and C/O of 0.55 (Asplund et al. 2009). Additional details about the simulations, i.e. initialization, runtime and the calculation of transmission spectra, are given in Appendix F.

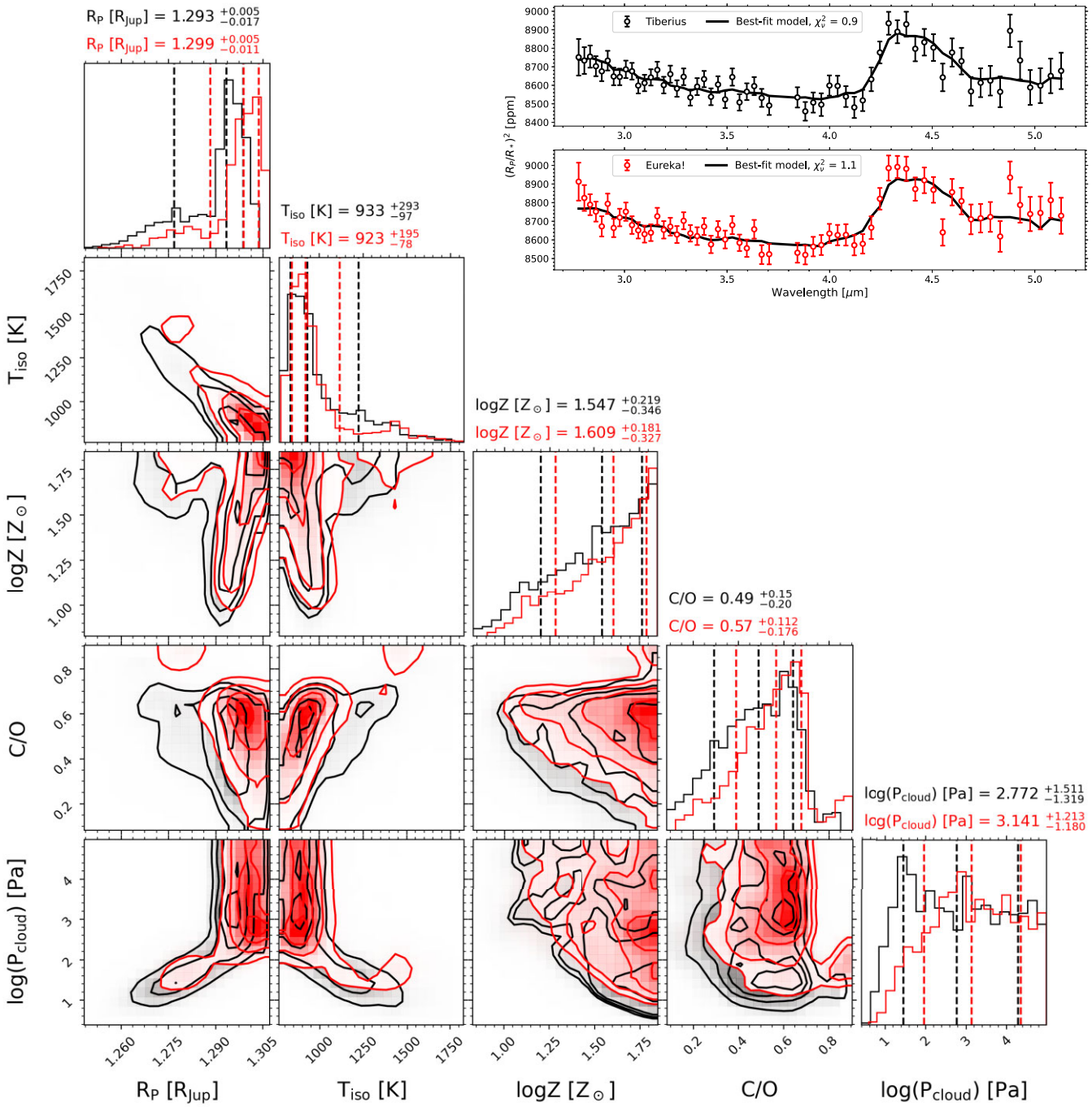

Figure 10. The corner plot and best-fitting models from our 1D chemical equilibrium atmosphere retrievals with PLATON run on the $R = 100$ spectra, after excluding the unphysically high metallicity solutions. The black contours correspond to the TIBERIUSretrieval and the red contours to the EUREKA! retrieval. The vertical dashed lines indicate the 16th, 50th (median), and 84th percentiles, which are also given in the axes titles.

Fig. 11 shows the comparison of WASP-15b's limb-average transmission spectra observed with *JWST* NIRSpec/G395H and predicted by the UM. For the purpose of this comparison, a vertical offset was applied to the UM spectra, the value of which was determined from the TIBERIUS reduction at $R = 100$ using a least-squares fit. The resulting offsets applied were -1523 ppm and -1515 ppm for the equilibrium and kinetics simulations, respectively. The results from the EUREKA! reduction are presented alongside those from TIBERIUS but were not used to obtain the applied offset values. Overall, this comparison demonstrates that the UM simulations predict the general shape of WASP-15b's limb-average transmission spectrum rather well. Both simulations suggest that H_2O, CO, and CO_2 are the major contributors to WASP-15b's opacity at the limbs. The enhancements in the observed transit depths at wavelengths where SO_2 and OCS absorb are not captured by the UM due to the lack of sulphur chemistry in the model.

Our GCM simulations suggest that the constraints on H_2O and CO_2 abundances, and by extension, on C/O, derived from *JWST*

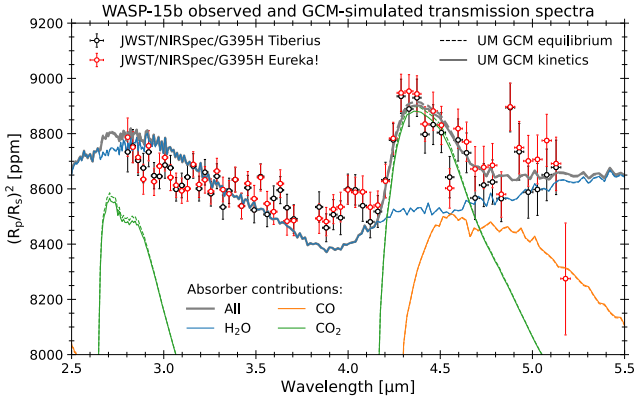

Figure 11. WASP-15b's $R = 100$ limb-averaged transmission spectra obtained using the TIBERIUS (black points) and EUREKA! (red points) reductions compared to the spectra predicted by the UM equilibrium (dashed lines) and kinetics (solid lines) simulations. UM simulations suggest that H_2O (blue lines), CO (orange lines), and CO_2 (green lines) are the major contributors to the observed limb-averaged transmission spectrum.

NIRSpec/G395H transit observations of planets like WASP-15b, could be informative not only in the context of the limbs of such planets but also in the context of their entire photospheres. To corroborate that we show the vertical profiles of major C- and O-bearing radiatively active species, CH_4, CO, CO_2, H_2O, and HCN (and NH_3 for completeness) predicted by the equilibrium and kinetics simulations in Fig. 12. First, we see that transport-induced quenching, a process capable of altering C and O budget and distribution at observable pressures in transmission (see Moses 2014, for review), causes CH_4, HCN, and NH_3 profiles in the kinetics simulation to diverge from those at chemical equilibrium: CH_4 is depleted while HCN and NH_3 abundances are enhanced at pressures lower than $\sim 10^{-1}$ bar. However, these disequilibrium changes in CH_4 and NH_3 would not cause the contributions of CH_4 and HCN to the overall absorption by C-bearing species in WASP-15b's photosphere to be much different from their contributions at chemical equilibrium, because *both* simulations predict that abundances of CH_4 and HCN are low (lower than 1 ppm) throughout the entire GCM model domain. Meanwhile, H_2O, CO, and CO_2 are more abundant than CH_4 and HCN in *both* simulations: H_2O and CO reach $\sim$10 000 ppm and $CO_2 \sim$10 ppm. H_2O, CO, and CO_2 are also rather uniformly distributed throughout the GCM model domain. Together, low CH_4 and HCN abundances but high H_2O, CO, and CO_2 abundances and their uniform spatial distribution, imply that H_2O, CO, and CO_2 would (1) account for the majority of C and O in WASP-15b's photosphere and (2) their contribution to the opacity at the limbs of the planet would be representative of their contribution to the opacity across the entire planet's photosphere.

As shown in Zamyatina et al. (2024), for WASP-96b, differences in metallicity and the assumption or relaxation of chemical equilibrium can produce differences in the spectra within the 3–5 μm range. However, these will largely manifest as differences in the applied vertical offset, which is not known and need not be the same across the two simulations, with differences as a function of wavelength being smaller than observational uncertainties. In light of our results in this work, we plan to revisit WASP-15b to explore, in more detail, the impacts of metallicity on the spectra within a 3D context, but this is beyond the scope of this work.

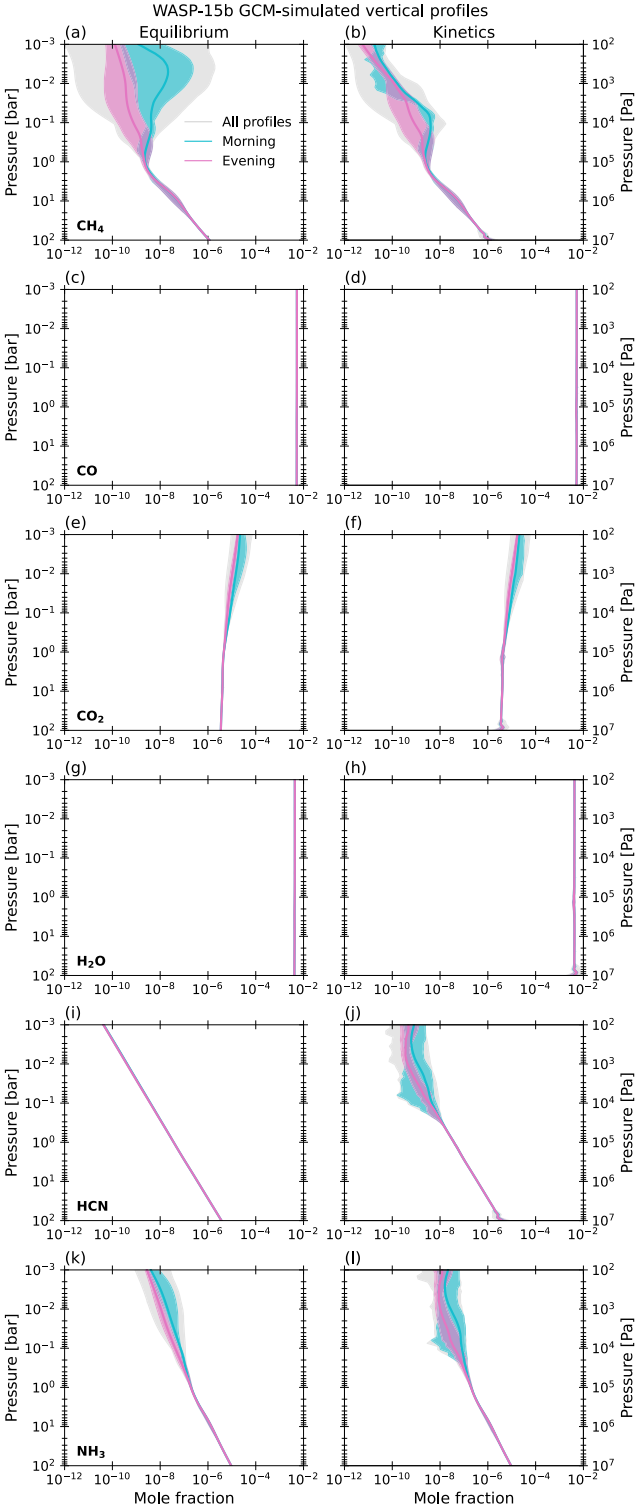

Figure 12. CH_4, CO, CO_2, H_2O, HCN, and NH_3 vertical profiles predicted by the UM equilibrium (left column) and kinetics (right column) simulations of WASP-15b's atmosphere. Grey shading shows the range of abundances for the entire atmosphere, cyan shading – for the morning terminator only, pink shading – for the evening terminator only. Solid cyan and pink lines indicate the meridional mean for the morning and evening terminator, respectively.

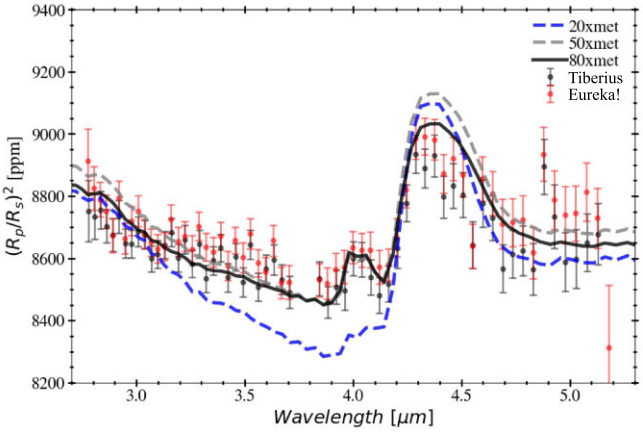

Figure 13. Photochemical model spectra for WASP-15b at 80× (solid, black), 50× (dashed, grey), and 20× (dashed, blue) solar metallicites as compared to the TIBERIUS (black points) and EUREKA! (red points) reductions. Photochemical models suggest that the observed SO_2 feature is indicative of a high metallicity atmosphere.

7 PHOTOCHEMICAL MODELLING

The evidence for absorption by SO_2 indicates that photochemistry is an active process in the atmosphere of WASP-15b. We model the photochemical processes in this atmosphere using VULCAN, a 1D kinetics model that treats photochemical (Tsai et al. 2021) and thermochemical (Tsai et al. 2017) reactions. The VULCAN set-up used in this work solves the Eulerian continuity equations, including chemical sources/sinks and diffusive transport. We use the updated C-H-N-O-S network[5] for hydrogen-dominated atmospheres that importantly considers S-bearing species.

We consider a grid of models based on the temperature profiles at the terminators of WASP-15b as calculated in the equilibrium UM GCM described in Section 6 and shown in Section G1. We use a K_{zz} profile based on the scaling relations in Moses et al. (2022) using an internal temperature of $T_{\rm int} = 100$ K. We use a host star stellar spectrum for a 6500 K star from the stellar spectral grid in Rugheimer et al. (2013), which combines synthetic ATLAS spectra (Kurucz 1979) with observed spectra from the International Ultraviolet Explorer for wavelengths less than 300 nm. We do not consider the impact of aerosol opacity in our models. The grid spans a range of planet metallicities from 10× solar, consistent with the input UM GCM, to 100× solar in intervals of 10. By extending to metallicities higher than those considered by our GCM model, we made the modelling trade-off of considering the differences in photochemistry on the terminators of WASP-15b based on the GCM modelling in-lieu of more self-consistent atmospheric modelling. To create spectra from the photochemical models, we use the PICASO radiative transfer code (Batalha et al. 2019) with a resolution of $R = 100$. The molecular opacities used to generate the transmission spectra in this work are taken from the references in Appendix G2.

Our photochemical models indicate that WASP-15b is likely to be substantially enhanced in metallicity compared to solar to reproduce the observed SO_2 feature, as shown in Fig. 13. To reproduce the amplitudes of all of the observed features, namely SO_2, H_2O, and CO_2, a metallicity of either $\sim 80\times$ solar or greater is preferred.

[5]https://github.com/exoclime/VULCAN/blob/master/thermo/SNCHO_photo_network_2024.txt

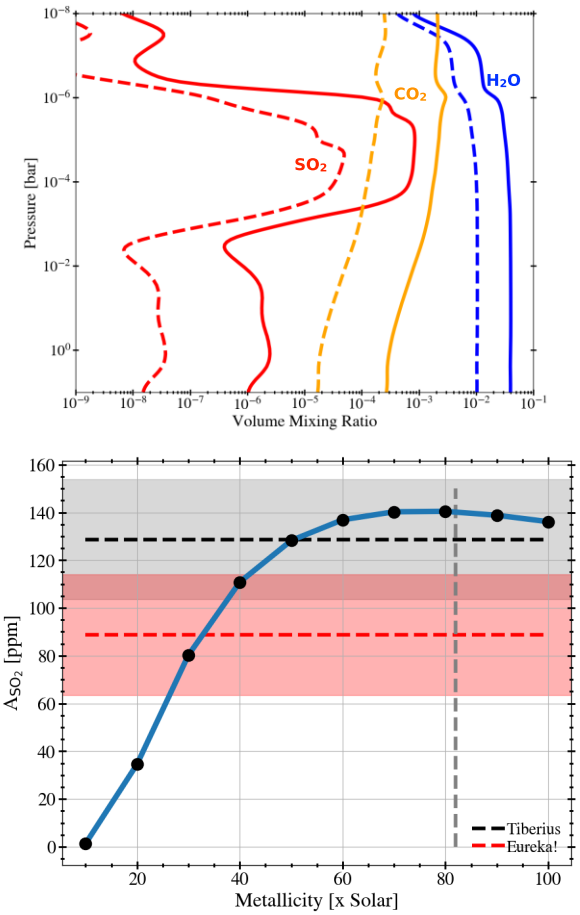

Figure 14. Top: the vertical distribution of SO_2, CO_2, and H_2O as predicted by the VULCAN photochemical model for an atmosphere with 80× solar metallicity (solid lines) and 20× solar metallicity (dashed lines). All three key species have abundances that change substantially with increased metallicity. Bottom: the predicted amplitude of the 4.05 μm feature (A_{SO_2}) varies by more than 100 ppm as a function of atmospheric metallicity. The observed amplitude and uncertainty of the feature are shown by the horizontal dashed lines and shaded regions for TIBERIUS (grey) and EUREKA! (red). This indicates a substantially metal-rich atmosphere based on our photochemical modelling. The vertical dashed grey line indicates the upper limit on the atmospheric metallicity derived from the interior structure model (Section 4).

We emphasize that the high metallicity required to reproduce the spectrum with photochemical modelling is driven by both the SO_2 and CO_2 feature amplitude (and to a lesser extent the H_2O feature amplitude as demonstrated in Section 5). Fig. 14 (bottom panel) shows how the amplitude of the SO_2 feature changes with metallicity as compared to the amplitude of the observed SO_2 feature. The abundance of SO_2 is highly sensitive to metallicity due to the net chemical reaction network that produces SO_2 which requires two H_2O molecules to interact with every H_2S molecule (Tsai et al. 2023; Powell et al. 2024). This effect can be seen in our model grid in Fig. 14 (top panel) where we find that the peak SO_2 abundance increases by more than an order of magnitude for substantially metal-rich atmospheres (e.g. 80× solar) as compared to more moderately enriched atmospheres (e.g. 20× solar).

We note that while both reductions are consistent with SO_2 amplitudes produced from models with lower metallicities than our 80× solar metallicity case, the CO_2 amplitude is systematically higher than our best-fitting 80× solar metallicity case for those lower

metallicity models (e.g. Fig. 13). However, there are two caveats to this high-metallicity interpretation. First, the GCM pressure–temperature profile that we use for our photochemical models (Appendix G1) may overly broaden the spectral features, pushing us to higher metallicities to fit the observed CO_2 feature. Secondly, these photochemical models do not include clouds. As we saw in our PETITRADTRANS forward models, the gradient of the H_2O feature can be fitted with cloud opacity, without the need for such high metallicities (Fig. 6).

The photochemical modelling results thus point towards a very high metallicity atmosphere for WASP-15b if the elements vary according to a solar abundance. Indeed, under the assumption of a cloud-free atmosphere, our photochemical models indicate that WASP-15b may have a metallicity near the maximum metallicity inferred from interior structure models (82× solar, Section 4). However, based on the SO_2 feature alone, our photochemical models are able to fit the amplitude of this feature with metallicities $\lesssim 40\times$ solar (Fig. 14, bottom panel). This is consistent with the metallicities inferred from our 1D retrievals which include clouds and a freely fitted, yet isothermal, temperature profile (Section 5). Future work that varies the individual abundance ratios of the different atomic species will be useful to better understand the chemistry of WASP-15b's atmosphere.

8 DISCUSSION

8.1 Differences between reductions and retrievals

Above, we presented inferences regarding WASP-15b's atmosphere from two different data reduction pipelines (Section 3) and three different retrieval models (Section 5). While all approaches are consistent with supersolar metallicity atmospheres and solar C/O, the spectra and retrieval results do have some differences. We discuss these differences in greater detail in the following sections.

8.1.1 Reduction differences

As stated in Section 3.3 there is an offset between the median transit depths of the $R = 100$ TIBERIUS and EUREKA! spectra. In Fig. 15, we present a comparison between the $R = 100$ spectra resulting from the two nominal reductions presented in Section 3 and additional test reductions. Considering first the difference between the nominal TIBERIUS (Section 3.1) and EUREKA! reductions (Section 3.2), we see there is both an offset and a slope in the NRS2 residuals (red line, Fig. 15).

A possible cause for this difference is the differing treatment of limb darkening. While both TIBERIUS and EUREKA! used quadratic limb darkening with coefficients informed by the same stellar parameters, 3D model and interpolation code, TIBERIUS fixed both $u1$ and $u2$ while EUREKA! fixed $u1$ and fitted for $u2$. In a separate test with TIBERIUS, we performed a fit where both limb-darkening coefficients were free parameters. This led to a transmission spectrum with a median depth 32 ppm deeper than the spectrum with fixed coefficients, which lessens the offset between EUREKA! and TIBERIUS, but did not lead to a slope difference in NRS2 (black dotted line, Fig. 15). Therefore, limb darkening could be partly, but not solely, responsible for the differences between TIBERIUS and EUREKA!.

An additional consideration is the role of the Stage 1 extraction, which includes the 1/f correction. The primary differences between the 1/f corrections of TIBERIUS and EUREKA! as implemented in this study are that TIBERIUS' is a row-by-row median correction while

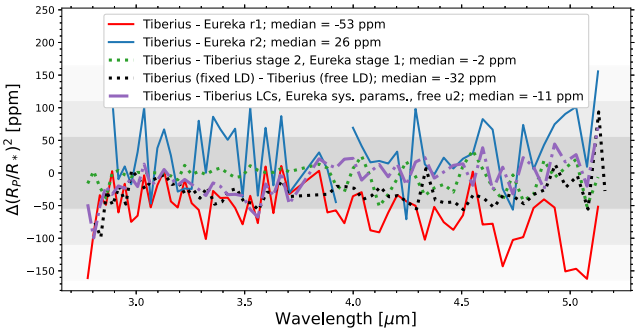

Figure 15. Figure showing the differences between the $R = 100$ spectra resulting from different reduction set-ups. In red is the difference between the nominal TIBERIUS (Section 3.1) and EUREKA! ('r1', Section 3.2) reductions. In blue is the difference between the nominal TIBERIUS reduction and the second EUREKA! reduction ('r2', Appendix B) which used the TIBERIUS Stage 1 out-puts. In dotted green is the difference between the nominal TIBERIUS reduction and a test TIBERIUS reduction run on the EUREKA! r1 Stage 1 outputs. In dotted black is a comparison between two TIBERIUS reductions with fixed versus completely free quadratic limb darkening, using an old binning scheme. In dot–dashed purple is a comparison between the nominal TIBERIUS reduction and a spectrum resulting from fitting the TIBERIUS light curves with the system parameters fixed to EUREKA! r1 and the second limb-darkening coefficient as a free parameter, to match the approach of EUREKA! r1. No offsets have been applied to any of these residuals. The grey shaded regions indicate 1×, 2×, and 3× the median transit depth uncertainty of the nominal TIBERIUS reduction.

EUREKA! applies the same Stage 3 background subtraction algorithm to the group-level files (after masking the trace). This means that EUREKA!'s correction has more free parameters and options to correct for 1/f noise, but can also introduce systematics, for example if outliers are not masked properly. In addition, EUREKA! also allows for a bias correction in the form of a multiplication factor that could explain some of the offsets between reductions.

We tested the impacts of the differing Stage 1 approaches in two different ways. First, we ran the TIBERIUS Stage 2 spectral extraction and light curve fitting on the EUREKA! Stage 1 outputs. This led to a transmission spectrum within 1σ of the nominal TIBERIUS reduction and a baseline offset of just 2 ppm (green dotted line, Fig. 15). Secondly, we performed an additional EUREKA! reduction (presented in Appendix B) which used TIBERIUS's Stage 1 output but EUREKA! from Stage 2 onwards. For this second EUREKA! reduction, we fixed both quadratic limb-darkening coefficients to the same values as TIBERIUS. This revealed a higher scatter in the residuals between this second EUREKA! reduction and the nominal TIBERIUS reduction (blue solid line, Fig. 15), and a median depth offset of +26 ppm but no slope in the NRS2 residuals. This suggests that the differences may be emerging at the Stage 2 (spectral extraction and light curve fitting) stage, including how limb darkening is treated.

Differences in the system parameters, namely a/R_* and i, can also lead to depth offsets and slopes between reductions (e.g. Alexoudi et al. 2018, 2020). As a final test, we ran a set of fits to the TIBERIUS light curves but fixing the NRS1/NRS2 system parameters to the NRS1/NRS2 best-fitting values from the nominal EUREKA! reduction (Table 1). In this test we also left the second limb darkening coefficient, $u2$, as a free parameter. This approach meant that we adopted the same fitting set-up as the nominal EUREKA! reduction but with the TIBERIUS light curves. Again, no slope difference was produced in NRS2's transmission spectrum (purple dash–dotted line, Fig. 15). Therefore, we do not believe differing system parameters are

the cause. Instead, this suggests differences in the light curves, which could be related to spectral extraction and/or background subtraction.

Although, we cannot conclusively determine the origins of the reduction differences, we are encouraged by the fact that despite these differences, our broad conclusions about the planet's supersolar metallicity and subsolar-to-solar C/O are not impacted (Section 5). However, we discuss specific retrieval differences in Section 8.1.2. Understanding the origins of reduction differences, such as slopes and offsets, is a broader problem faced by the community as a whole (e.g. Carter et al. 2024). Thus far there is no consensus on best practices, in particular, because these effects seem to vary between stellar types and brightnesses, planet types, instruments used, etc. Further investigation is needed to understand the origins of these differences and if and how they may impact population-level atmospheric inferences. In the meantime, the BOWIE-ALIGN approach is to have at least two independent reductions and retrievals per planet and one uniform reduction set-up threading through all planets' analyses. The independent approaches will allow us to assess the robustness and uncertainties of our inferences while the uniform approach should allow us to mitigate biases arising from different approaches when we combine our results at the end of our survey (Kirk et al. 2024a).

8.1.2 *Retrieval differences*

When comparing the results between retrieval codes, it is important to consider how each code defines its parameters. For example PETITRADTRANS's chemical equilibrium models parametrize metallicity as [Fe/H] with chemical equilibrium grids calculated over a range of [Fe/H]. However, when adjusting the C and O abundances, PETITRADTRANS scales C/H with metallicity and then sets O/H according to C/O. PLATON takes the opposite approach, adjusting O/H based on metallicity, Z ([M/H]), and then setting C/H based on C/O. The approach of both PETITRADTRANS and PLATON means that (C+O)/H does not respect scaled metallicity abundances.

Furthermore, in our PETITRADTRANS retrievals, we included the planet's surface gravity as a free parameter with a Gaussian prior. PLATON does not include the surface gravity as a fit parameter, instead allowing the planet mass to be a fit parameter (in addition to the planet radius). In our PLATON retrievals, we fix the planet's mass and only fit for the radius. In a further test, we ran a retrieval with mass as a fit parameter with a Gaussian prior from Bonomo et al. (2017) but found this made no difference to our resulting posteriors. With regard to the cloud-top pressure, PLATON recovers a lower pressure cloud deck than PETITRADTRANS, albeit with large uncertainties. However, this is misleading as the PLATON corner plot (Fig. 10) shows that the cloud-top pressure is actually unconstrained with a lower limit of $\gtrsim 10$ Pa (0.1 mbar). It is important to note that the reference pressure is fixed to 1 mbar in our PETITRADTRANS retrievals and to 1 bar in our PLATON retrievals.

Of the different PETITRADTRANS set-ups, we favour the 'hybrid chemistry' retrievals owing to their better fits to the data (Fig. 7). These follow equilibrium chemistry, but with the addition of free abundances for SO_2 and OCS. However, all PETITRADTRANSapproaches produce consistent results (Table E1).

Fig. 16 shows the contributions of gas and cloud opacities from the best-fitting hybrid and free chemistry retrievals to the TIBERIUS $R = 100$ spectrum. This figure demonstrates how the relatively shallow gradient of the H_2O feature drives the hybrid model to include CH_4 and the free chemistry model to include grey cloud opacity. This same shallow NRS1 slope is likely responsible for driving the PLATON and

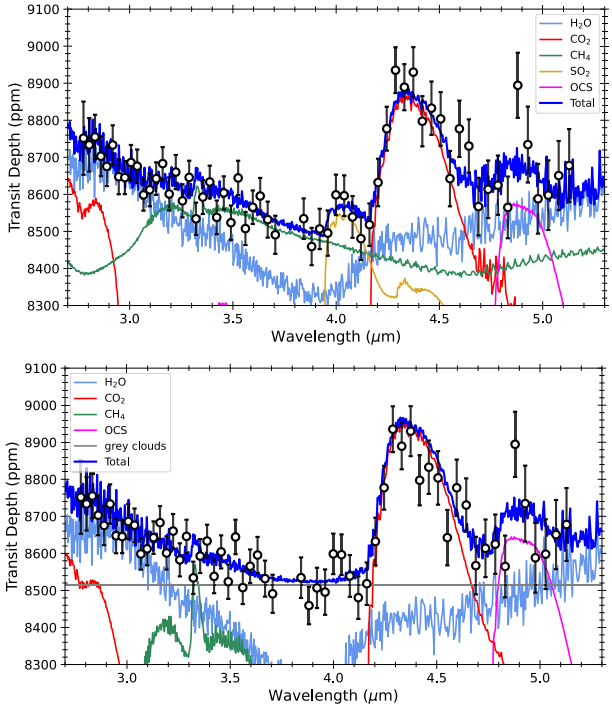

Figure 16. Figure showing the contributions of opacities from the best-fitting PETITRADTRANS hybrid chemistry (equilibrium plus free S) retrieval (top panel) and free chemistry retrieval (bottom panel) to the TIBERIUS $R = 100$ spectrum. The difference in Bayesian evidences, $\Delta \ln Z$, is 2.7 in favour of the hybrid model (top panel).

BEAR retrievals to high metallicities. As we saw in Section 5.2, the Bayesian evidence favours the hybrid and equilibrium models over free chemistry by $\sim 3\sigma$ for TIBERIUS and the hybrid model over free chemistry by $\sim 4\sigma$ for EUREKA!.

From our retrievals, the isothermal temperatures converge to temperatures that are 600–700 K cooler than the equilibrium temperature of the planet (1676 ± 29 K), albeit with large uncertainties. Considering only the PETITRADTRANS retrievals, we see that the hybrid retrievals favour isothermal temperatures of around 900 K while the free retrievals find temperatures around 1100 K (Table E1). This could be why these two retrievals disagree at to whether CH_4 or clouds are needed to fit the NRS1 data (Fig. 16).

Retrieved temperatures are often cooler than the equilibrium temperatures. This can be caused both by the assumption of 1D atmospheres that neglect limb asymmetries (MacDonald, Goyal & Lewis 2020) and modelling choices, such as how the pressure–temperature profile is parametrized (Welbanks & Madhusudhan 2022). Our three retrieval set-ups with PETITRADTRANS (Section 5.2), BEAR (Section 5.3), and PLATON (Section 5.4) all used isothermal pressure–temperature profiles. Our GCM model predicts maximal differences of ~ 100 ppm in the amplitude of CO_2 between the morning and evening limbs (Fig. 12). Therefore, the cool temperatures we retrieve may be a product of both our pressure–temperature parametrization (Welbanks & Madhusudhan 2022) and real thermal limb asymmetries (MacDonald et al. 2020).

So far, our retrieval approaches have neglected the possibility of a transit depth offset between NRS1 and NRS2 (Section 8.1.1). To correct this, we ran a further two PLATON retrievals on the nominal TIBERIUS (Section 3.1) and EUREKA! (Section 3.2) reductions but this time with an additional free parameter that fits for a transit

depth offset between NRS1 and NRS2. This offset parameter had a uniform prior bounded between −200 and +200 ppm. For TIBERIUS, the resulting offset was consistent with zero (14^{+21}_{-20} ppm) and hence there was no significant difference in the posteriors of the other parameters ($Z = 35^{+23}_{-19}\times$ solar, no offset; $Z = 29^{+33}_{-18}\times$ solar, with offset; $\mathrm{C/O} = 0.49^{+0.15}_{-0.20}$, no offset; $\mathrm{C/O} = 0.43^{+0.18}_{-0.21}$, with offset). The Bayesian evidence difference between the TIBERIUS retrievals with and without an offset was less than 1, indicating no statistical preference for a depth offset between NRS1 and NRS2. For EUREKA!, the resulting offset was 52^{+22}_{-21} ppm. This led to a slightly larger change in the retrieved Z and C/O but neither of which was statistically significant ($Z = 41^{+21}_{-22}\times$ solar, no offset; $Z = 32^{+31}_{-19}\times$ solar, with offset; $\mathrm{C/O} = 0.57^{+0.11}_{-0.18}$, no offset; $\mathrm{C/O} = 0.38^{+0.19}_{-0.21}$, with offset). For EUREKA!, the Bayesian evidence difference was 5 in favour of the retrieval with an offset, indicating a $> 3\sigma$ preference (e.g. Benneke & Seager 2013).

Despite these differences, we are encouraged by the fact that our conclusion regarding the planet's supersolar metallicity and subsolar-to-solar C/O is not impacted. To help the community consolidate our suite of reductions and retrievals, we recommend the use of the results from the PETITRADTRANS hybrid chemistry retrievals run on the TIBERIUS spectra. This is because the TIBERIUS spectrum does not require a depth offset and our PETITRADTRANS hybrid chemistry retrievals allow for disequilibrium sulphur chemistry (which PLATON does not) and do not suffer the high metallicity problems of BEAR and PLATON.

8.2 WASP-15b's atmospheric composition and predictions from migration scenarios

Despite the differences in abundances retrieved by each code (Table E1), they consistently point towards a supersolar metallicity and an approximately solar C/O ratio. Our GCM simulations (Section 6), that included C-O-N-H gas-phase chemistry and assumed aerosol-free conditions, suggest that CO, H_2O and CO_2 are the most abundant C- and O-bearing chemical species in WASP-15b's atmosphere. This supports our use of NIRSpec/G395H to measure the planet's C/O from its H_2O and CO_2 features. Given that these GCM simulations also predict that the spatial distribution of CO, H_2O and CO_2 is rather uniform throughout the entire GCM model domain (with CO_2 variations in the vertical being less than an order of magnitude; Fig. 12), this suggests that CO, H_2O and CO_2's contribution to the opacity at the limbs of the planet is representative of their contribution to the opacity across the entire planet's photosphere.

As explained in the introduction, WASP-15b is part of our ongoing survey (Kirk et al. 2024a) to determine whether aligned and misaligned hot Jupiters around F stars have different C/O ratios and metallicities based on their likely different migration mechanisms (disc versus disc-free/high-eccentricity). As shown in Penzlin & Booth et al. 2024, without the full BOWIE-ALIGN sample we cannot make conclusive statements about where the planet formed due to lack of knowledge of where C and O are in the solids; however, the misaligned nature and high metallicity allow us to speculate in general terms.

WASP-15b is a misaligned hot Jupiter, which suggests it formed exterior to ~ 0.6 au and underwent disc-free (high-eccentricity) migration (Muñoz et al. 2016). The supersolar metallicity we infer for WASP-15b indicates the late accretion of solids, which would serve to drive up the O/H of its atmosphere (Booth et al. 2017; Schneider & Bitsch 2021). The fact that we also see evidence for sulphur content (Section 8.3), additionally points to the planet acquiring its high metallicity via the accretion of solids rather than high metallicity gas (Chachan et al. 2023). This is because sulphur in the disc is bound in solids and thus cannot be delivered by metal-rich gas accretion (Danti, Bitsch & Mah 2023), except at temperatures too high to be compatible with high-eccentricity migration (above ~ 700 K; Lodders 2003; Timmermann et al. 2023). Given the mass of WASP-15b is much larger than the pebble isolation mass ($\sim 20\,M_\oplus$, Bitsch et al. 2018), the planet likely only had minor pebble accretion late in its formation, implying planetesimal accretion as the main driver of the solid enrichment.

Alternatively, the planet's composition may be explained without the accretion of planetesimals if WASP-15b accreted its envelope more-or-less *in situ*. Here, pebbles might be small enough to be accreted alongside the gas (Morbidelli, Batygin & Lega 2023), possibly enabling a high metallicity. Further, metal-rich gas accretion could explain the planet's composition if the accretion happened close enough to the star that refractory sulphur sublimates. While *in situ* formation of hot Jupiters is often disfavoured (e.g. Dawson & Johnson 2018), composition alone cannot rule out this scenario if an alternative explanation for the misaligned orbit of the planet can be found.

We find a C/O ratio in the range 0.4–0.6, which is consistent with the solar C/O. However, there is no clear interpretation of where the planet formed because the amount of carbon and oxygen contained in solids is unknown. As shown in Penzlin & Booth et al. 2024, the prospects for such analyses may be better once the full sample of planets is available. This is one of the main goals of our observational programme (Kirk et al. 2024a).

8.3 Sulphur chemistry in WASP-15b's atmosphere

As described in Sections 5.2 and 7, the absorption features we see at 4.0 and 4.9 μm can be fit with SO_2 and OCS, respectively. We discuss the plausibility of this sulphur chemistry below.

First, we compared WASP-15b to the ERS observations of the Saturn-mass planet WASP-39b which resulted in the first detection of SO_2 in an exoplanet's atmosphere (Alderson et al. 2023; Rustamkulov et al. 2023; Tsai et al. 2023). Since this detection in WASP-39b, there have been additional detections of SO_2 in the atmospheres of the Neptune-mass planet WASP-107b (Dyrek et al. 2024; Sing et al. 2024; Welbanks et al. 2024), the sub-Neptune GJ 3470b (Beatty et al. 2024), and hints of SO_2 in the sub-Neptune TOI-270d (Benneke et al. 2024; Holmberg & Madhusudhan 2024).

The abundance of SO_2 seen in WASP-39b's spectrum was several orders of magnitude higher than expectations based on equilibrium chemistry. This implies that photochemistry is responsible for the observed abundance of SO_2, with the reaction chain beginning with the photodissociation of water in the planet's atmosphere (Tsai et al. 2023). This is why our equilibrium chemistry models, that do not include photochemistry, do not attempt to fit the 4.0 μm feature in WASP-15b's spectrum (Figs 6, 7, 10 and 11). Given that WASP-15b orbits an earlier spectral type star than WASP-39b (F7, Triaud et al. 2010, versus G8, Faedi et al. 2011), and is more irradiated ($T_{\rm eq} = 1676 \pm 29$ K, Southworth et al. 2013, versus $T_{\rm eq} = 1116^{+33}_{-32}$ K, Faedi et al. 2011), it is likely that photochemistry is also important for its atmosphere.

To determine the amplitude of SO_2 absorption in WASP-15b's atmosphere relative to WASP-39b, we plot the NIRSpec/G395H transmission spectrum of WASP-39b from Alderson et al. (2023) along with WASP-15b's transmission spectrum in Fig. 17. For this comparison, we binned the WASP-39b spectrum to $R = 100$ and then scaled the transit depths of both WASP-39b and WASP-15b by the transit depth corresponding to one scale height for both

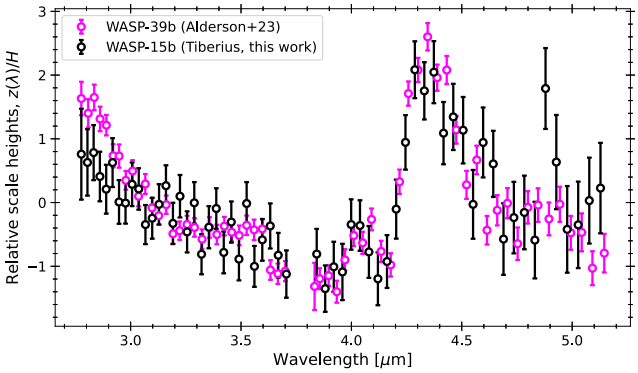

Figure 17. The transmission spectrum of WASP-15b (black, this work) as compared with that of WASP-39b (magenta, Alderson et al. 2023) binned to $R = 100$. The transmission spectra have been scaled with respect to the planets' atmospheric scale heights.

planets (421 ppm for WASP-39b and 139 ppm for WASP-15b). This figure indicates that the amplitude of the SO_2 absorption in both planets is approximately one atmospheric scale height. For WASP-39b, the smaller spectral uncertainties, resulting from the planet's larger scale height, led to a 4.8σ detection of SO_2 while our larger uncertainties for WASP-15b prevent a statistically significant detection. Follow-up observations of WASP-15b would improve the spectral precision and could search for additional SO_2 absorption features in the mid-infrared (Powell et al. 2024).

Our hybrid PETITRADTRANS retrievals place upper limits on the abundance of SO_2 in WASP-15b's atmosphere of $\lesssim 100$ ppm (Fig. 8), while the forward models favour an abundance of ~ 5 ppm (Section 5.1). This abundance of SO_2 would be consistent with the abundances seen in the modestly supersolar metallicity WASP-39b (0.5–25 ppm; Powell et al. 2024) and WASP-107b (6–9 ppm; Dyrek et al. 2024; Sing et al. 2024; Welbanks et al. 2024) but somewhat smaller than the 270^{+220}_{-120} ppm seen in the $125 \pm 40\times$ solar metallicity GJ 3470b. This is consistent with expectations that SO_2 abundance is correlated with metallicity (Tsai et al. 2023).

The most notable difference between the spectra of WASP-39b and WASP-15b is the feature at 4.9 μm which is only present in WASP-15b's spectrum. This absorption feature appears in both the TIBERIUS and EUREKA! spectra at $R = 100$ and $R = 400$ (Fig. 4). The feature is confined to a single bin (= 61 pixels) at $R = 100$ and a handful of bins in the $R = 400$ spectrum. By fitting a Gaussian to the $R = 400$ transmission spectrum at these wavelengths, we determine that this feature has a central wavelength of 4.90 μm and a full width at half maximum of 0.05 μm.

We investigated whether this feature is correlated to any unusual behaviour in limb darkening, systematics coefficients, excess red and white noise, and excess bad pixels at these wavelengths. We found no correlation between any of these parameters and the outliers at these wavelengths. Given these tests, and the fact that the absorption feature is independently seen in both the TIBERIUS and EUREKA! reductions, we conclude that this is a real absorption feature.

To interpret what may be the cause of this feature, we explored a number of different molecules that would be present in both chemical equilibrium and disequilibrium, including CH_4, CO, H_2S, HCN, O_3, PH_3, NH_3, C_2H_2, SO_2, NO, HC_3N, H_2CO, CS_2, SO, SH, OCS, OH, AlH, AlO, CaH, CrH, FeH, MgH, MgO, NaH, SiO, and SiO2. Of these molecules, the only ones that matched the wavelength of the feature we see are OCS and O_3 (ozone). We ruled out O_3 based on the feature width (O_3 would result in a much broader feature) and the implausibility of finding the large abundances of O_3 necessary to match the feature strength in a H_2-dominated atmosphere.

In Fig. 7, we showed how the inclusion of OCS in our free and hybrid retreivals with PETITRADTRANS leads to a better fit of the 4.9 μm absorption feature. However, this figure also showed that the width of the feature at 4.9 μm is narrower than expected for OCS. We investigated if the narrowness of the feature could be caused by OCS at lower pressures or temperatures than the bulk atmospheric composition responsible for the other spectral features. To do this, we ran the PETITRADTRANS forward model with an abundance of OCS localized between 1 and 100 μbar, and attempted to vary the temperature and OCS abundance in this part of the atmosphere to fit the feature. A temperature of 300 K with a 2 per cent OCS mixing ratio in this part of the atmosphere gave a feature that was still slightly broader and weaker than the feature observed in the $R = 400$ spectrum. Such a cold temperature and high abundance of OCS localized to the upper part of the atmosphere of WASP-15b is highly unphysical.

Aside from the quality of the fits, there are caveats regarding the physics of the OCS interpretation, namely that OCS is not expected to be abundant at the low pressures ($\lesssim$ mbar) probed by transmission (Tsai et al. 2021, 2023). Similar to H_2S, OCS is destroyed by photodissociation as well as by photochemically produced atomic H and atomic S. To have OCS at the high altitudes we are observing, either the photochemical sinks must be suppressed, or there exist unidentified production mechanisms. Jordan et al. (2021) found that OCS can survive at high altitudes in a Venus-like atmosphere around M stars with significantly lower NUV flux. However, OCS is expected to be depleted around F-type stars like WASP-15 or even stars with solar-like UV radiation. Alternatively, it is conceivable that OCS might be produced through the oxidation of CS or CS_2 after their formation in the upper atmosphere, although the abundances of CS and CS_2 remain low in our models. The identification of plausible OCS production is beyond the scope of this study.

In summary, we believe that the absorption we see at 4.9 μm is astrophysical and not an instrumental artefact. While OCS is the leading candidate, there are several caveats to this interpretation. Alternatively, the feature observed at 4.9 μm could be produced by a molecule not included in currently available line lists, necessitating additional laboratory work (Fortney et al. 2019).

9 CONCLUSIONS

We present the 2.8–5.2 μm transmission spectrum of the misaligned hot Jupiter WASP-15b obtained from a single transit observation with *JWST*/NIRSpec/G395H. We reduce our data with three independent approaches and find minimal red noise in our data, likely due to the quiet and relatively faint star which allows for a high number groups per integration (44). This allows us to measure a precise transmission spectrum (median uncertainty of 55 ppm at $R = 100$ and 106 ppm at $R = 400$).

We interpret WASP-15b's spectrum using three independent retrieval codes and GCM simulations. Our spectrum reveals significant absorption from H_2O (4.9σ) and CO_2 (8.9σ), with evidence for SO_2 and absorption at 4.9 μm for which the current best candidate is OCS, albeit with several caveats. If further observations of this planet are able to confirm if the feature at 4.9 μm is indeed OCS this would be the first detection of this molecule in an exoplanet atmosphere and would allow for new tests of sulphur chemistry in exoplanet atmospheres.

Despite some differences between the absolute abundances inferred from which reduction and retrieval code is adopted, all

methods converge on a supersolar metallicity atmosphere ($\gtrsim 15\times$ solar) and a C/O that is consistent with solar but with relatively large uncertainties. Our GCM simulations for WASP-15b suggest that the C/O we measure at the limb is likely representative of the entire photosphere due to the mostly uniform spatial distribution of H_2O, CO_2, and CO.

The supersolar metallicity we infer for WASP-15b indicates the late accretion of planetesimals. The fact that we also see evidence for sulphur content, may additionally point to planetesimal accretion as sulphur cannot be delivered by metal-rich gas accretion in the inner disc (Bitsch, Schneider & Kreidberg 2022). Given the mass of WASP-15b is much larger than the pebble isolation mass, it likely only had minor pebble accretion late in its formation, instead implying planetesimal accretion as the main driver of solid enrichment. However, we refrain from making comparisons between the planet's C/O and formation models, such as those of Penzlin & Booth et al. 2024, until we have analysed the rest of the planets in our programme (Kirk et al. 2024a), as these comparisons need to be performed for a sample of planets rather than individual objects.

This is the first planet to be observed as part of our BOWIE-ALIGN programme that seeks to determine whether a hot Jupiter's atmospheric composition depends on its method of migration, as indicated by its obliquity around an F star (GO 3838, PIs: Kirk & Ahrer, Kirk et al. 2024a). By combining WASP-15b with the results from the rest of our programme, we will test models of planet formation and demonstrate whether atmospheric composition can be reliably traced to formation history.

ACKNOWLEDGEMENTS

The authors thank Bertram Bitsch for insightful discussion and the anonymous reviewer whose suggestions made our comparative analyses more impactful and our conclusions more robust. This work is based on observations made with the National Aeronautics and Space Administration (NASA) / European Space Agency (ESA) / Canadian Space Agency (CSA) *JWST*. The data were obtained from the Mikulski Archive for Space Telescopes at the Space Telescope Science Institute, which is operated by the Association of Universities for Research in Astronomy, Inc., under NASA contract NAS 5–03127 for *JWST*. These observations are associated with program #3838. This work was inspired by collaboration through the UK-led BOWIE+ collaboration. JK acknowledges financial support from Imperial College London through an Imperial College Research Fellowship grant. NJM, DES, and MZ acknowledge support from a UK Reseach and Innovation (UKRI) Future Leaders Fellowship (Grant MR/T040866/1), a Science and Technology Facilities Funding Council Nucleus Award (Grant ST/T000082/1), and the Leverhulme Trust through a research project grant (RPG-2020-82). RAB thanks the Royal Society for their support through a University Research Fellowship. PJW acknowledges support from the UKRI Science and Technology Facilities Council (STFC) through consolidated grant ST/X001121/1. VP acknowledges support from the UKRI Future Leaders Fellowship grant MR/S035214/1 and STFC through the consolidated grant ST/X001121/1.

DATA AVAILABILITY

The data products associated with this manuscript can be found online at Zenodo at https://doi.org/10.5281/zenodo.14779026. We describe the data products resulting from our survey in Kirk et al. (2024a).

REFERENCES

Abel M., Frommhold L., Li X., Hunt K. L. C., 2011, J. Phys. Chem. A, 115, 6805
Abel M., Frommhold L., Li X., Hunt K. L. C., 2012, J. Chem. Phys., 136, 044319
Ahrer E.-M. et al., 2023, Nature, 614, 653
Albrecht S. et al., 2012, ApJ, 757, 18
Alderson L., Grant D., Wakeford H., 2022, Exo-TiC/ExoTiC-JEDI: v0.1-beta-release, Zenodo, available at: https://zenodo.org/records/7185855
Alderson L. et al., 2023, Nature, 614, 664
Alexoudi X. et al., 2018, A&A, 620, A142
Alexoudi X., Mallonn M., Keles E., Poppenhäger K., von Essen C., Strassmeier K. G., 2020, A&A, 640, A134
Amundsen D. S., Baraffe I., Tremblin P., Manners J., Hayek W., Mayne N. J., Acreman D. M., 2014, A&A, 564, 1
Amundsen D. S. et al., 2016, A&A, 595, A36
Amundsen D. S., Tremblin P., Manners J., Baraffe I., Mayne N. J., 2017, A&A, 598, 1
Asplund M., Grevesse N., Sauval A. J., Scott P., 2009, ARA&A, 47, 481
Azzam A. A. A., Tennyson J., Yurchenko S. N., Naumenko O. V., 2016, MNRAS, 460, 4063
Banerjee A. et al., 2024, ApJ, 975, L11
Barber R., Strange J., Hill C., Polyansky O., Mellau G. C., Yurchenko S., Tennyson J., 2014, MNRAS, 437, 1828
Batalha N. E., Marley M. S., Lewis N. K., Fortney J. J., 2019, ApJ, 878, 70
Beatty T. G. et al., 2024, ApJ, 970, L10
Bell T. J. et al., 2022, J. Stat. Softw., 7, 4503
Benneke B., Seager S., 2013, ApJ, 778, 153
Benneke B. et al., 2024, preprint (arXiv:2403.03325)
Bitsch B., Morbidelli A., Johansen A., Lega E., Lambrechts M., Crida A., 2018, A&A, 612, A30
Bitsch B., Schneider A. D., Kreidberg L., 2022, A&A, 665, A138
Bonomo A. S. et al., 2017, A&A, 602, A107
Booth R. A., Clarke C. J., Madhusudhan N., Ilee J. D., 2017, MNRAS, 469, 3994
Brady R. P., Yurchenko S. N., Tennyson J., Kim G.-S., 2024, MNRAS, 527, 6675
Buchner J. et al., 2014, A&A, 564, A125
Carter A. L. et al., 2024, Nat. Astron., 8, 1008
Chachan Y., Knutson H. A., Lothringer J., Blake G. A., 2023, ApJ, 943, 112
Christie D. A., Mayne N. J., Zamyatina M., Baskett H., Evans-Soma T. M., Wood N., Kohary K., 2024, MNRAS, 532, 3001
Chubb K. L. et al., 2021, A&A, 646, A21
Claringbold A., Rimmer P., Rugheimer S., Shorttle O., 2023, AJ, 166, 39
Coles P. A., Yurchenko S. N., Tennyson J., 2019, MNRAS, 490, 4638
Danti C., Bitsch B., Mah J., 2023, A&A, 679, L7
Dawson R. I., Johnson J. A., 2018, ARA&A, 56, 175
Dobbs-Dixon I., Cowan N. B., 2017, ApJ, 851, L26
Drummond B. et al., 2020, A&A, 636, A68
Dyrek A. et al., 2024, Nature, 625, 51
Edwards J. M., 1996, J. Atmos. Sci., 53, 1921
Edwards J. M., Slingo A., 1996, Q. J. R. Meteorol. Soc., 122, 689
Espinoza N., Fortney J. J., Miguel Y., Thorngren D., Murray-Clay R., 2017, ApJ, 838, L9
Faedi F. et al., 2011, A&A, 531, A40
Fairman C., Wakeford H. R., MacDonald R. J., 2024, AJ, 167, 240
Faure A., Wiesenfeld L., Drouin B. J., Tennyson J., 2013, J. Quant. Spec. Radiat. Transf., 116, 79
Feinstein A. D. et al., 2023, Nature, 614, 670
Feroz F., Hobson M. P., 2008, MNRAS, 384, 449
Ford E. B., Rasio F. A., 2008, ApJ, 686, 621
Foreman-Mackey D., Hogg D. W., Lang D., Goodman J., 2013, PASP, 125, 306
Fortney J. et al., 2019, Astro2020: Decadal Survey on Astronomy and Astrophysics, 2020, 146
Gaia Collaboration, 2016, A&A, 595, A1

Gaia Collaboration, 2023, A&A, 674, A1
Gordon I. E. et al., 2017, J. Quant. Spec. Radiat. Transf., 203, 3
Goyal J. M. et al., 2020, MNRAS, 498, 4680
Grant D., Wakeford H. R., 2024, J. Open Source Softw., 9, 6816
Helling C. et al., 2016, MNRAS, 460, 855
Holmberg M., Madhusudhan N., 2024, A&A, 683, L2
Huang X., Gamache R. R., Freedman R. S., Schwenke D. W., Lee T. J., 2014, J. Quant. Spectrosc. Radiat. Transf., 147, 134
Jakobsen P. et al., 2022, A&A, 661, A80
Jordan S., Rimmer P. B., Shorttle O., Constantinou T., 2021, ApJ, 922, 44
JWST Transiting Exoplanet Community Early Release Science Team, 2023, Nature, 614, 649
Kipping D. M., Tinetti G., 2010, MNRAS, 407, 2589
Kirk J., Wheatley P. J., Louden T., Doyle A. P., Skillen I., McCormac J., Irwin P. G. J., Karjalainen R., 2017, MNRAS, 468, 3907
Kirk J. et al., 2021, AJ, 162, 34
Kirk J. et al., 2024a, RASTI, 3, 691
Kirk J. et al., 2024b, AJ, 167, 90
Kitzmann D., Heng K., Oreshenko M., Grimm S. L., Apai D., Bowler B. P., Burgasser A. J., Marley M. S., 2020, ApJ, 890, 174
Kreidberg L., 2015, PASP, 127, 1161
Kurucz R. L., 1979, ApJS, 40, 1
Law C. J. et al., 2021, ApJS, 257, 3
Lenzuni P., Chernoff D. F., Salpeter E. E., 1991, ApJS, 76, 759
Li G., Gordon I. E., Rothman L. S., Tan Y., Hu S.-M., Kassi S., Campargue A., Medvedev E. S., 2015, ApJS, 216, 15
Lightkurve Collaboration, 2018, Astrophysics Source Code Library, record ascl: 1812.013
Lines S. et al., 2018, MNRAS, 481, 194
Lodders K., 2003, ApJ, 591, 1220
MacDonald R. J., Goyal J. M., Lewis N. K., 2020, ApJ, 893, L43
Madhusudhan N., Amin M. A., Kennedy G. M., 2014, ApJ, 794, L12
Magic Z., Chiavassa A., Collet R., Asplund M., 2015, A&A, 573, A90
Mayne N. J., Baraffe I., Acreman D. M., Smith C., Wood N., Amundsen D. S., Thuburn J., Jackson D. R., 2014a, Geosci. Model Dev., 7, 3059
Mayne N. J. et al., 2014b, A&A, 561, A1
Mollière P., van Boekel R., Dullemond C., Henning T., Mordasini C., 2015, ApJ, 813, 47
Mollière P., van Boekel R., Bouwman J., Henning T., Lagage P.-O., Min M., 2017, A&A, 600, A10
Mollière P., Wardenier J., Van Boekel R., Henning T., Molaverdikhani K., Snellen I., 2019, A&A, 627, A67
Moran S. E. et al., 2023, ApJ, 948, L11
Morbidelli A. et al., 2016, Icarus, 267, 368
Morbidelli A., Batygin K., Lega E., 2023, A&A, 675, A75
Morello G., Zingales T., Martin-Lagarde M., Gastaud R., Lagage P.-O., 2021, AJ, 161, 174
Moses J. I., 2014, Phil. Trans. R. Soc. A, 372, 20130073
Moses J. I., Tremblin P., Venot O., Miguel Y., 2022, Exp. Astron., 53, 279
Müller S., Helled R., 2024, ApJ, 967, 7
Muñoz D. J., Lai D., Liu B., 2016, MNRAS, 460, 1086
Nasedkin E., Mollière P., Blain D., 2024, J. Open Source Softw., 9, 5875
Öberg K. I., Murray-Clay R., Bergin E. A., 2011, ApJ, 743, L16
Owen J. E., 2020, MNRAS, 495, 3160
Owens A., Yurchenko S. N., Tennyson J., 2024, MNRAS, 530, 4004
Patel J. A., Espinoza N., 2022, AJ, 163, 228
Penzlin A. B. T. et al., 2024, MNRAS, 535, 171
Polyansky O. L., Kyuberis A. A., Zobov N. F., Tennyson J., Yurchenko S. N., Lodi L., 2018, MNRAS, 480, 2597
Powell D. et al., 2024, Nature, 626, 979
Rajpurohit A. S., Reylé C., Allard F., Homeier D., Schultheis M., Bessell M. S., Robin A. C., 2013, A&A, 556, A15
Rasio F. A., Ford E. B., 1996, Science, 274, 954
Rothman L. S. et al., 2010, J. Quant. Spec. Radiat. Transf., 111, 2139
Rugheimer S., Kaltenegger L., Zsom A., Segura A., Sasselov D., 2013, Astrobiology, 13, 251
Rustamkulov Z. et al., 2023, Nature, 614, 659
Saumon D., Marley M. S., Abel M., Frommhold L., Freedman R. S., 2012, ApJ, 750, 74
Schneider A. D., Bitsch B., 2021, A&A, 654, A71
Sing D. K. et al., 2024, Nature, 630, 831
Skilling J., 2004, Fischer R., in Preuss R., von Toussaint U., eds, AIP Conf. Ser., Vol. 735, Bayesian Inference and Maximum Entropy Methods in Science and Engineering. Am. Inst. Phys., New York, p. 395
Skrutskie M.F. et al., 2006, AJ, 131, 1163
Southworth J. et al., 2013, MNRAS, 434, 1300
Speagle J. S., 2020, MNRAS, 493, 3132
Tashkun S. A., Perevalov V. I., 2011, J. Quant. Spec. Radiat. Transf., 112, 1403
Taylor J. et al., 2023, MNRAS, 524, 817
Thorngren D. P., Fortney J. J., 2018, AJ, 155, 214
Thorngren D., Fortney J. J., 2019, ApJ, 874, L31
Thorngren D. P., Fortney J. J., Murray-Clay R. A., Lopez E. D., 2016, ApJ, 831, 64
Timmermann A., Shan Y., Reiners A., Pack A., 2023, A&A, 676, A52
Triaud A. H. M. J. et al., 2010, A&A, 524, A25
Trotta R., 2008, Contem. Phys., 49, 71
Tsai S.-M., Lyons J. R., Grosheintz L., Rimmer P. B., Kitzmann D., Heng K., 2017, ApJS, 228, 20
Tsai S.-M., Malik M., Kitzmann D., Lyons J. R., Fateev A., Lee E., Heng K., 2021, ApJ, 923, 264
Tsai S.-M. et al., 2023, Nature, 617, 483
Underwood D. S., Tennyson J., Yurchenko S. N., Huang X., Schwenke D. W., Lee T. J., Clausen S., Fateev A., 2016, MNRAS, 459, 3890
Vardya M. S., 1962, ApJ, 135, 303
Venot O., Bounaceur R., Dobrijevic M., Hébrard E., Cavalié T., Tremblin P., Drummond B., Charnay B., 2019, A&A, 624, A58
Virtanen P. et al., 2020, Nat. Methods, 17, 261
Wakeford H. R. et al., 2018, AJ, 155, 29
Welbanks L., Madhusudhan N., 2022, ApJ, 933, 79
Welbanks L. et al., 2024, Nature, 630, 836
West R. G. et al., 2009, AJ, 137, 4834
Wilzewski J. S., Gordon I. E., Kochanov R. V., Hill C., Rothman L. S., 2016, J. Quant. Spectrosc. Radiat. Transf, 168, 193
Woitke P., Helling C., Hunter G. H., Millard J. D., Turner G. E., Worters M., Blecic J., Stock J. W., 2018, A&A, 614, A1
Wood N. et al., 2014, Q. J. R. Meteorol. Soc., 140, 1505
Wu Y., Murray N., 2003, ApJ, 589, 605
Yurchenko S. N., Tennyson J., 2014, MNRAS, 440, 1649
Yurchenko S. N., Tennyson J., Barber R. J., Thiel W., 2013, J. Mol. Spectrosc., 291, 69
Yurchenko S. N., Amundsen D. S., Tennyson J., Waldmann I. P., 2017, A&A, 605, A95
Yurchenko S. N., Mellor T. M., Freedman R. S., Tennyson J., 2020, MNRAS, 496, 5282
Zamyatina M. et al., 2023, MNRAS, 519, 3129
Zamyatina M. et al., 2024, MNRAS, 529, 1776
Zhang M., Chachan Y., Kempton E. M. R., Knutson H. A., 2019, PASP, 131, 034501
Zhang M., Chachan Y., Kempton E. M. R., Knutson H. A., Chang W. H., 2020, ApJ, 899, 27

APPENDIX A: ALLAN VARIANCE PLOTS FOR SPECTROSCOPIC LIGHT CURVES

This appendix includes the Allan variance plots for the spectroscopic light curves from both the TIBERIUS and EUREKA! reductions in Fig. A1.

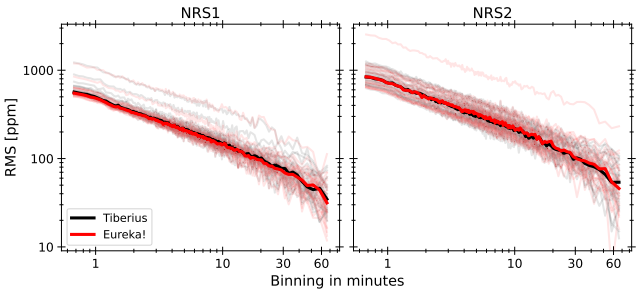

Figure A1. The Allan variance plot from the TIBERIUS (black) and EUREKA! (red) $R = 100$ spectroscopic light curve fits for NRS1 (left panel) and NRS2 (right panel). The thick lines show the median Allan variances.

APPENDIX B: SECOND EUREKA! REDUCTION

As mentioned in Section 3, we performed a second, independent reduction with EUREKA! to determine how robust our spectrum is to choices made during the spectral extraction process. Aside from a different choice of wavelength binning to generate the spectroscopic light curves, the key difference between this second reduction and the EUREKA! reduction presented in Section 3 is that we start with the Stage 1 output of TIBERIUS as described in Section 3 and use them as inputs to the Stage 2 of EUREKA!. We perform the spectral extraction in EUREKA!'s Stage 3 the same way as done in Section 3 except we use a $> 10\sigma$ threshold for performing the double-iterative masking of outliers along the time axis, extract the background from the area >10 pixels away from central pixel of the trace, and use a full width of 8 pixels for optimal spectral extraction. For the light curve fitting, we followed the same steps in the first reduction as described in Section 3, except we fixed both the quadratic limb-darkening parameters u1 and u2 to the `ExoTiC-LD` values.

We present the comparison between the spectra from both EUREKA! reductions and the TIBERIUS reduction in Fig. B1. This figure shows that the spectra from each reduction are consistent with one another. Unlike in Fig. 4, no transit depth offset has been applied between the spectra in this plot. The differences in the median transit depths are: EUREKA!r1 – TIBERIUS= 38 ppm, EUREKA! r2 – TIBERIUS= −17 ppm (in the overlapping wavelength range, ≥ 2.9 μm). These differences are both less than the median transit depth uncertainties of each spectrum: EUREKA! r1 = 54 ppm, TIBERIUS= 54 ppm, EUREKA! r2 = 61 ppm.

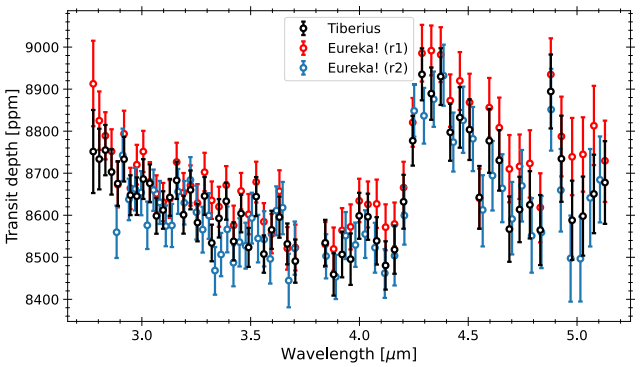

Figure B1. The comparison between the transmission spectra obtained with TIBERIUS (black), EUREKA! reduction 1 (red, Section 3), and EUREKA! reduction 2 (blue).

APPENDIX C: TESS LIGHT CURVE FITTING

Given the lack of optical wavelength coverage from our G395H transmission spectrum, we decided to fit the *TESS* light curves. Our goal was to place a constraint on the transit depth at visible wavelengths which could help constrain cloud and haze parameters (e.g. Wakeford et al. 2018; Fairman, Wakeford & MacDonald 2024). Rather than taking the literature *TESS* transit depth for WASP-15b (Patel & Espinoza 2022), we re-fitted the *TESS* light curve with the values for the system parameters (T_0, a/R_*, i) that we derived from our *JWST* light curves (TIBERIUS values, Table 1). This was done to avoid a bias in the transit depth arising from inconsistent system parameters.

We used `lightkurve` (Lightkurve Collaboration 2018) to extract the short cadence (SPOC) *TESS* light curve and phase-folded this using the period from Patel & Espinoza (2022) and the T_0 from our own *JWST* light curve fits. We trimmed the phase-folded *TESS* light curve to have the same out-of-transit baseline as our *JWST* data and fitted the trimmed light curve using a `batman` model multiplied by a linear polynomial to be consistent with our *JWST* light curve fits. The resulting R_P/R_* we derive from the *TESS* light curve is 0.092155 ± 0.000470 ($(R_P/R_*)^2 = 8493 \pm 87$ ppm), which is within 1σ of Patel & Espinoza (2022) but is more precise owing to the fewer free parameters in our model. However, despite this improved precision, the inclusion of the *TESS* data did not improve the precision of our retrievals and did not substantially change the fit of the GCM spectra to our *JWST* data, so we opted against using the *TESS* data in our final analysis.

APPENDIX D: NIGHTSIDE DILUTION CALCULATION

To determine the amplitude of dilution in the transmission spectrum caused by thermal emission from the planet's nightside, we used both the equations from Kipping & Tinetti (2010) and the EXOTETHYS package (Morello et al. 2021). EXOTETHYS additionally accounts for dilution from the planet's phase curve variations over the course of a transit observation. Both approaches give consistent results, with the dilution amplitude ranging from 5 ppm at the bluest wavelengths we consider to 14 ppm at the reddest wavelengths. These variations are significantly smaller than the uncertainties in our $R = 100$ spectra and so we do not apply a dilution correction to our final transmission spectrum.

APPENDIX E: PARAMETERS AND ADDITIONAL PLOTS FROM ATMOSPHERIC RETRIEVALS

This appendix includes the tabulated parameters from our 1D atmospheric retrievals (Section 5). We also include a PETITRADTRANS corner plot for the free retrievals (Fig. E1), the BEAR $R = 100$ best fit and corner plot without the restricted metallicity (Fig. E2) and the PLATON corner plot without the restricted metallicity (Fig. E3).

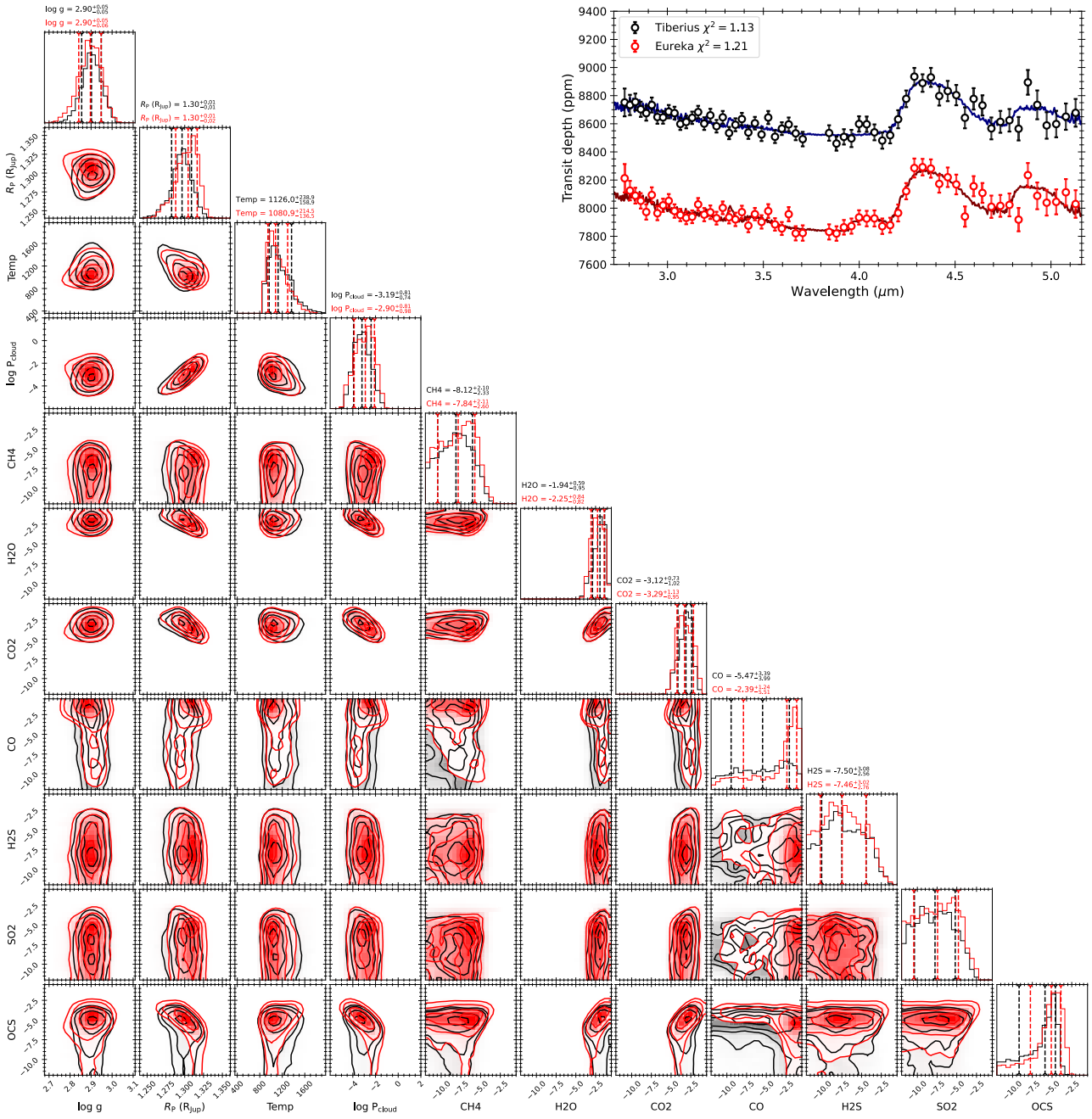

Figure E1. Corner plot showing the posterior PDFs from the free petitradtrans retrieval performed on the TIBERIUS $R = 100$ spectrum (black) and EUREKA! $R = 100$ spectrum (red). The best fitting model and residuals are displayed in the top right.

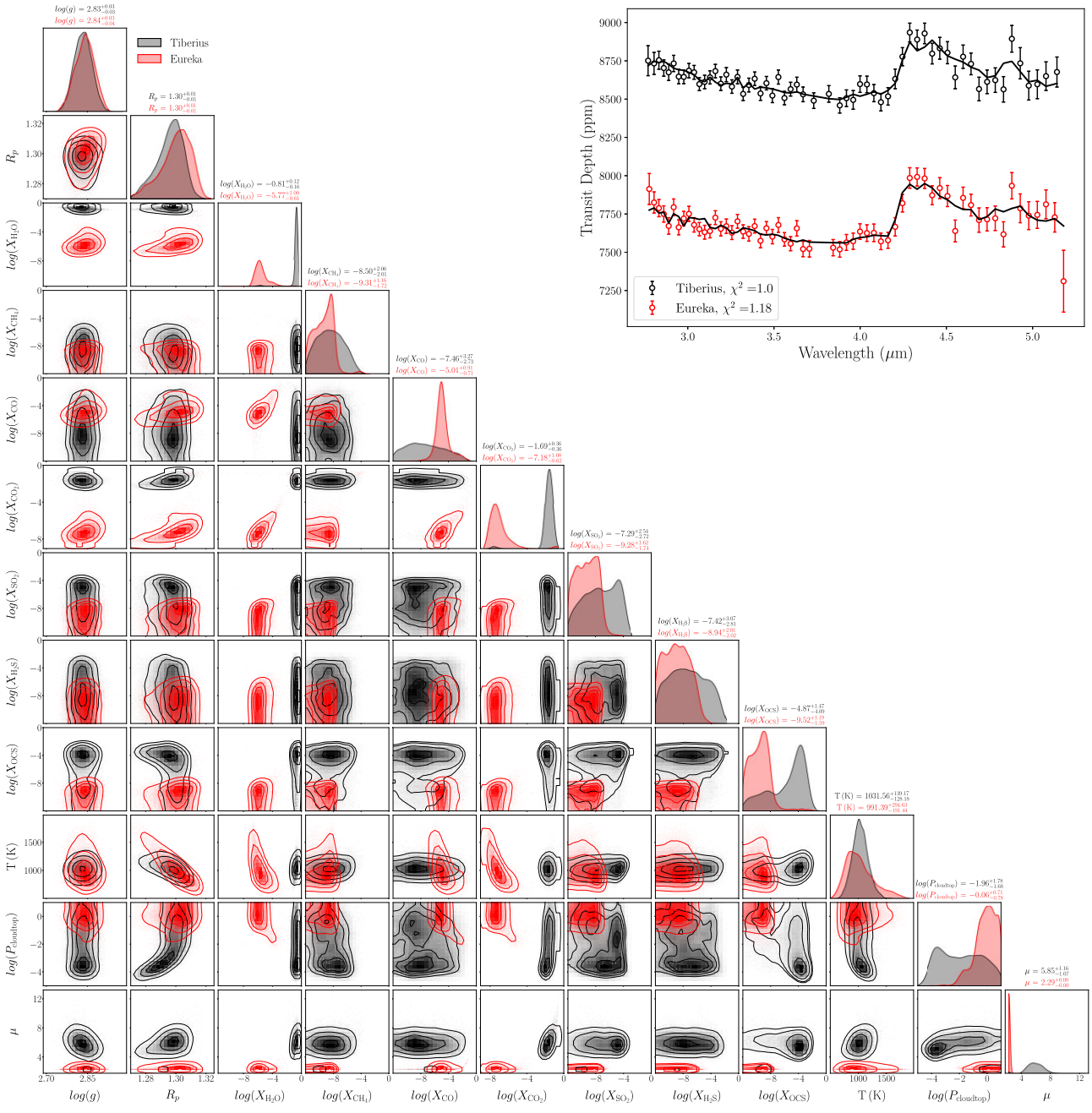

Figure E2. Corner plot showing the posteriors from the BEAR retrievals on the TIBERIUS (black) and EUREKA! (red) reductions of WASP-15 b at $R = 100$ prior to excluding the high mean molecular weight solutions. Note that the mean molecular weight, μ, is not a free parameter in the retrievals, but is derived from the retrieved abundances. The top right insert shows the best-fitting models for the TIBERIUS (black) and EUREKA! (red) reductions. The EUREKA! spectrum is offset by 1000 ppm for visualization purposes. The legend in the bottom left indicates the reduced χ^2 values for each of the fits.

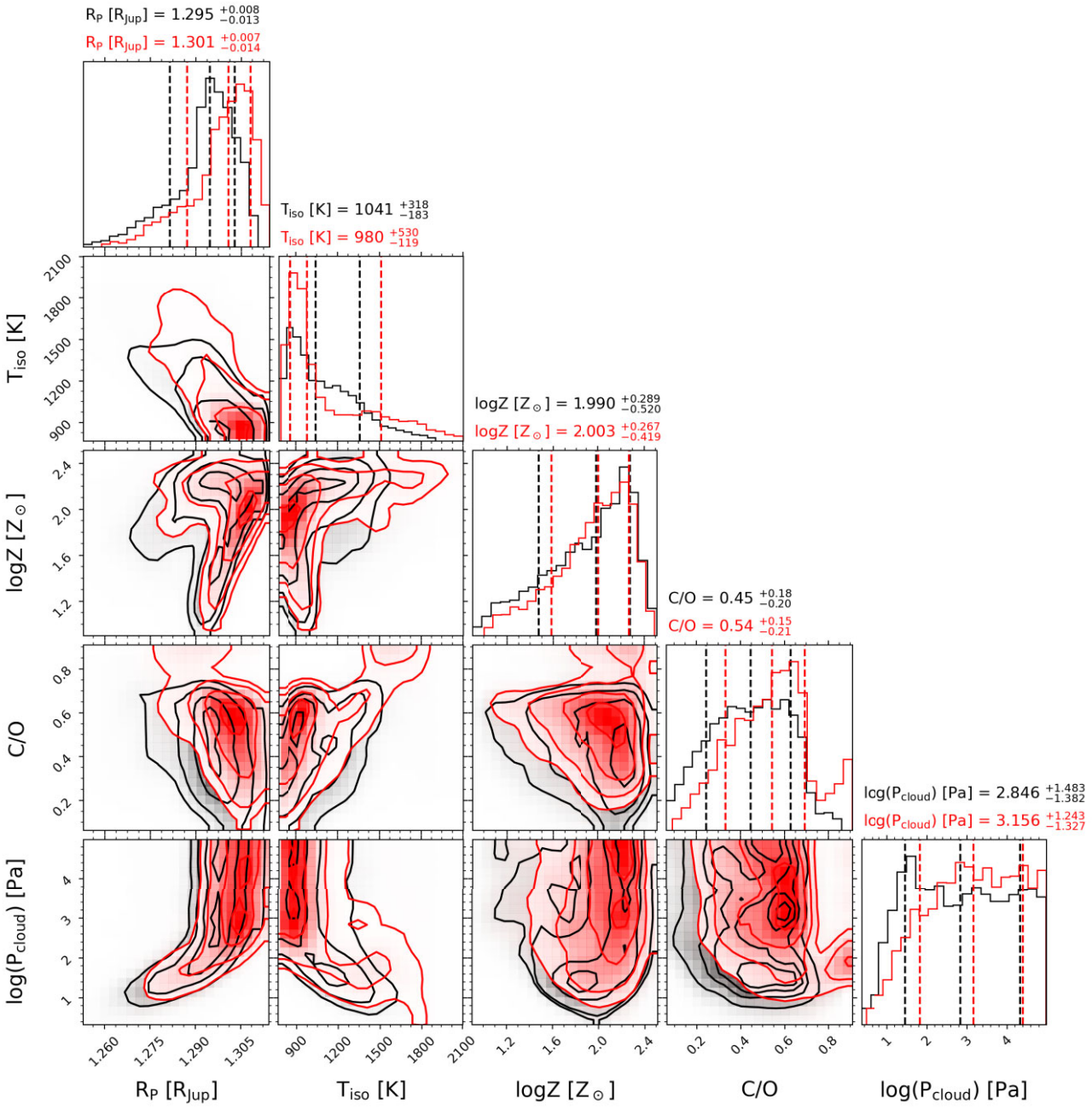

Figure E3. The corner plot from our 1D chemical equilibrium atmosphere retrievals with PLATON run on the $R = 100$ spectra over the full, unrestricted metallicity prior range [−1,3]. The black contours correspond to the TIBERIUS retrieval and the red contours to the EUREKA! retrieval. The vertical dashed lines indicate the 16th, 50th (median), and 84th percentiles, which are also given in the axes titles.

Table E1. The results from our retrievals using PETITRADTRANS (free and equilibrium chemistry, Section 5.2), BEAR (free chemistry, Section 5.3) and PLATON (equilibrium chemistry, Section 5.4). In this table, the PETITRADTRANS abundances have been converted from the mass fractions presented in the PETITRADTRANS corner plots. Both BEAR and PLATON include additional rows where the posteriors have been recalculated after excluding solutions with $Z > 82\times$ solar, motivated by our interior structure model (Section 4). For the BEAR retrievals this is limited to the $R = 100$ case, as removing the high metallicity solutions from the $R = 400$ retrievals does not leave sufficient posterior samples. Parameters that are not fit parameters for each code are marked as '–'.

Input spectrum	R_P (R_J)	log g (cgs)	T_{iso} (K)	log P_{cloud} (bar)	Z (× solar)	C/O	$\log(X_{H_2O})$	$\log(X_{CO_2})$	$\log(X_{CO})$	$\log(X_{SO_2})$	$\log(X_{OCS})$
PETITRADTRANS											
Equilibrium Chemistry:											
TIBERIUS, $R = 100$	1.302 ± 0.003	2.88 ± 0.05	910^{+110}_{-73}	$-0.50^{+1.61}_{-2.04}$	18^{+22}_{-8}	$0.48^{+0.11}_{-0.16}$	–	–	–	–	–
EUREKA!, $R = 100$	1.305 ± 0.002	$2.87^{+0.05}_{-0.04}$	914^{+86}_{-62}	$-0.45^{+1.62}_{-1.76}$	22^{+27}_{-9}	$0.53^{+0.09}_{-0.16}$	–	–	–	–	–
Free Chemistry:											
TIBERIUS, $R = 100$	1.296 ± 0.013	2.90 ± 0.05	1126^{+239}_{-159}	$-3.19^{+0.81}_{-0.74}$	–	–	$-2.83^{+0.59}_{-0.95}$	$-4.40^{+0.73}_{-1.02}$	$-6.55^{+3.39}_{-3.99}$	$-9.20^{+2.56}_{-2.61}$	$-7.31^{+1.31}_{-3.29}$
EUREKA!, $R = 100$	1.304 ± 0.002	$2.90^{+0.05}_{-0.06}$	1081^{+215}_{-137}	$-2.90^{+0.81}_{-0.98}$	–	–	$-3.14^{+0.84}_{-0.82}$	$-4.57^{+1.13}_{-0.95}$	$-3.48^{+1.24}_{-5.51}$	$-8.88^{+2.64}_{-3.02}$	$-6.52^{+1.22}_{-2.64}$
Hybrid Chemistry:											
TIBERIUS, $R = 100$ *	1.306 ± 0.002	$2.87^{+0.04}_{-0.05}$	887^{+65}_{-56}	$-0.66^{+1.78}_{-1.83}$	22^{+20}_{-10}	$0.53^{+0.09}_{-0.15}$	–	–	–	$-6.56^{+1.11}_{-4.46}$	$-8.84^{+2.04}_{-3.10}$
TIBERIUS, $R = 400$	1.306 ± 0.002	2.87 ± 0.05	882 ± 58	$-0.65^{+1.76}_{-1.90}$	17^{+14}_{-8}	$0.51^{+0.10}_{-0.16}$	–	–	–	$-7.13^{+1.54}_{-4.14}$	$-9.14^{+2.09}_{-2.72}$
EUREKA!, $R = 100$	1.303 ± 0.002	2.84 ± 0.05	891^{+47}_{-49}	$-0.48^{+1.68}_{-1.78}$	24^{+19}_{-11}	$0.56^{+0.07}_{-0.13}$	–	–	–	$-5.49^{+0.34}_{-1.63}$	$-6.52^{+0.65}_{-2.15}$
EUREKA!, $R = 400$	1.303 ± 0.002	$2.85^{+0.04}_{-0.05}$	882^{+43}_{-46}	$-0.63^{+1.75}_{-1.70}$	22^{+16}_{-9}	$0.57^{+0.07}_{-0.12}$	–	–	–	$-5.53^{+0.35}_{-1.87}$	$-6.90^{+0.76}_{-3.25}$
BEAR											
Full prior range:											
TIBERIUS, $R = 100$	$1.297^{+0.007}_{-0.01}$	2.83 ± 0.03	1031^{+139}_{-128}	$-1.96^{+1.78}_{-1.68}$	–	–	$-0.81^{+0.12}_{-0.16}$	-1.69 ± 0.36	$-7.46^{+3.27}_{-2.73}$	$-7.29^{+2.54}_{-2.72}$	$-4.87^{+1.47}_{-4.09}$
TIBERIUS, $R = 400$	1.302 ± 0.007	2.84 ± 0.03	1163^{+212}_{-192}	$-1.46^{+1.39}_{-1.38}$	–	–	$-0.82^{+0.15}_{-0.29}$	$-1.13^{+0.23}_{-0.2}$	$-7.59^{+3.2}_{-2.67}$	$-7.99^{+2.28}_{-2.21}$	$-7.69^{+2.3}_{-2.44}$
EUREKA!, $R = 100$	$1.301^{+0.008}_{-0.011}$	$2.84^{+0.03}_{-0.04}$	991^{+294}_{-191}	$-0.06^{+0.71}_{-0.78}$	–	–	$-5.77^{+1.0}_{-0.61}$	$-7.18^{+1.08}_{-0.62}$	$-5.01^{+0.91}_{-0.71}$	$-9.28^{+1.62}_{-1.74}$	$-9.52^{+1.19}_{-1.59}$
EUREKA!, $R = 400$	$1.296^{+0.01}_{-0.011}$	2.84 ± 0.03	1498^{+274}_{-292}	$-2.09^{+1.58}_{-1.37}$	–	–	$-0.91^{+0.16}_{-0.32}$	$-0.98^{+0.16}_{-0.14}$	$-6.5^{+3.27}_{-3.36}$	$-7.77^{+2.62}_{-2.57}$	$-7.1^{+3.17}_{-2.94}$
High Z solutions excluded											
TIBERIUS, $R = 100$	1.291 ± 0.007	2.84 ± 0.03	1169^{+190}_{-198}	$0.11^{+0.53}_{-0.81}$	–	–	$-5.79^{+0.4}_{-0.47}$	$-7.44^{+0.5}_{-0.32}$	$-7.13^{+1.27}_{-2.58}$	$-9.79^{+1.42}_{-1.29}$	$-9.06^{+0.68}_{-1.6}$
EUREKA!, $R = 100$	$1.301^{+0.008}_{-0.011}$	$2.84^{+0.03}_{-0.04}$	992^{+298}_{-190}	$-0.03^{+0.69}_{-0.74}$	–	–	$-5.79^{+0.85}_{-0.59}$	$-7.22^{+0.9}_{-0.6}$	$-5.02^{+0.83}_{-0.67}$	$-9.32^{+1.6}_{-1.71}$	$-9.59^{+1.15}_{-1.54}$
PLATON											
Full prior range:											
TIBERIUS, $R = 100$	$1.295^{+0.008}_{-0.013}$	–	1041^{+318}_{-183}	$-3.846^{+1.483}_{-1.382}$	97^{+92}_{-68}	$0.45^{+0.18}_{-0.20}$	–	–	–	–	–
TIBERIUS, $R = 400$	$1.300^{+0.006}_{-0.008}$	–	1016^{+310}_{-175}	$-2.280^{+1.173}_{-1.391}$	162^{+77}_{-92}	$0.45^{+0.17}_{-0.20}$	–	–	–	–	–
EUREKA!, $R = 100$	$1.301^{+0.007}_{-0.014}$	–	980^{+530}_{-119}	$-2.156^{+1.243}_{-1.327}$	100^{+85}_{-62}	$0.54^{+0.15}_{-0.21}$	–	–	–	–	–
EUREKA!, $R = 400$	$1.304^{+0.005}_{-0.008}$	–	960^{+285}_{-93}	$-2.440^{+1.067}_{-1.242}$	123^{+78}_{-71}	$0.57^{+0.10}_{-0.18}$	–	–	–	–	–
High Z solutions excluded											
TIBERIUS, $R = 100$	$1.293^{+0.005}_{-0.017}$	–	933^{+293}_{-97}	$-3.772^{+1.511}_{-1.319}$	35^{+23}_{-19}	$0.49^{+0.15}_{-0.20}$	–	–	–	–	–
TIBERIUS, $R = 400$	$1.299^{+0.003}_{-0.005}$	–	852^{+84}_{-54}	$-2.539^{+0.915}_{-1.216}$	44^{+18}_{-21}	$0.51^{+0.12}_{-0.19}$	–	–	–	–	–
EUREKA!, $R = 100$	$1.299^{+0.005}_{-0.011}$	–	923^{+195}_{-78}	$-2.141^{+1.213}_{-1.180}$	41^{+21}_{-22}	$0.57^{+0.11}_{-0.18}$	–	–	–	–	–
EUREKA!, $R = 400$	$1.300^{+0.003}_{-0.005}$	–	915^{+77}_{-61}	$-2.469^{+1.010}_{-1.018}$	42^{+19}_{-21}	$0.61^{+0.07}_{-0.15}$	–	–	–	–	–

* Our favoured interpretation for the reasons discussed in Section 8.1.2.

APPENDIX F: ADDITIONAL DETAILS ABOUT THE UM

F1 WASP-15 system parameters used in the UM simulations

Tables F1 and F2 show the stellar and planetary parameters, respectively, used in the UM simulations presented in this study.

F2 UM initialization and runtime

The UM equilibrium simulation was performed first. We initialized this simulation at rest with a piecewise power-law pressure–temperature profile crudely approximating the results from initial tests with analytic chemistry. This simulation was then ran for 1500 Earth days to let the upper atmosphere (from 10^{-3} bar to 1 bar) reach a pseudo-steady state dynamically, radiatively and chemically. The UM kinetics simulation was initialized from day 1000 of the UM equilibrium simulation, and ran for another 1000 Earth days.

F3 Constructing UM high resolution transmission spectrum

During normal UM runtime, radiative transfer is computed for 32 spectral bands covering 0.2 to 322 μm. During diagnostic UM runs required to obtain a planet's transmission spectrum (Lines et al. 2018), radiative transfer was computed at a higher spectral resolution for two sets of spectral bands, (1) 500 spectral bands covering 0.2 to 10 000 μm and (2) 500 spectral bands covering 0.2 to 10 000 μm. The resulting two high resolution transmission spectra were combined into one high resolution spectrum via post-processing.

Table F1. WASP-15 parameters used in the UM simulations.

Parameter	Value	Unit
Type	F7	
Radius	10.03×10^{8} [a]	m
Effective temperature	6300 [b]	K
Stellar constant at 1 au	4235.10	$W\,m^{-2}$
$\log_{10}$(surface gravity)	4.00 [c]	Gal (cgs)
[Fe/H]	0.00 [d]	dex

[a] $10.03 \times 10^8 = 1.48\,R_\odot \approx 1.477 \pm 0.072\,R_\odot$ (Bonomo et al. 2017).
[b] 6300 K ≈ 6372 ± 13 K (Gaia Collaboration 2023).
[c] 4.00 (cgs) ≈ 4.17 (cgs) (Bonomo et al. 2017).
[d] 0.00 ≈ −0.17 (Bonomo et al. 2017).

Table F2. WASP-15b parameters used in the UM simulations.

Parameter	Value	Unit
Inner radius	9.07×10^{7} [a]	m
Domain height	1.50×10^{7} [a]	m
Semimajor axis	0.0520 [b]	au
Orbital period	3.7521 [c]	Earth day
Rotation rate	1.94×10^{-05}	$rad\,s^{-1}$
Surface gravity at inner radius	8.30 [d]	$m\,s^{-2}$
Intrinsic temperature	300	K
Metallicity [M/H]	10×solar	Asplund et al. (2009)
C/O	0.55	Asplund et al. (2009)
Specific gas constant	3256.02	$J\,K^{-1}\,kg^{-1}$
Specific heat capacity	1.25×10^{04}	$J\,K^{-1}\,kg^{-1}$
Stellar irradiance	1.57×10^{06}	$W\,m^{-2}$
Effective temperature	1555 [e]	K

Notes:[a] $(9.07 + 1.50) \times 10^7$ m $= 1.06 \times 10^8$ m $= 1.48\,R_J$.
[b] 0.0520 au ≈ 0.05165 au (Southworth et al. 2013).
[c] 3.7521 Earth day ≈ 3.75209748 Earth day (Southworth et al. 2013).
[d] With the inner radius boundary initially placed at 200 bar.
[e] Calculated at pseudo-steady state as $(OLR/\sigma)^{1/4}$, where OLR is the global mean top-of-the-atmosphere outgoing longwave radiation and σ is the Stefan–Boltzmann constant.

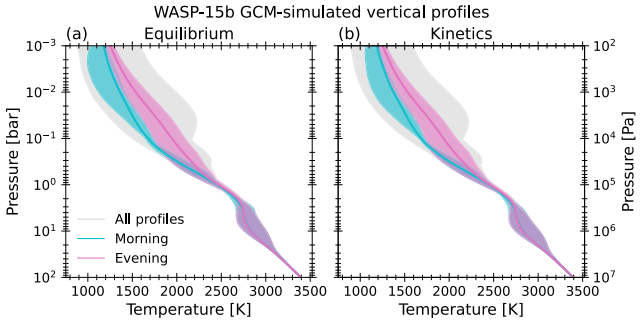

Figure F1. Pressure–temperature vertical profiles predicted by the UM equilibrium (left column) and kinetics (right column) simulations of WASP-15b's atmosphere. Grey shading shows the range of abundances for the entire atmosphere, cyan shading – for the morning terminator only, pink shading – for the evening terminator only. Solid cyan and pink lines indicate the meridional mean for the morning and evening terminator, respectively.

F4 UM pressure–temperature and chemical species vertical profiles

Fig. F1 shows pressure–temperature profiles predicted by the UM equilibrium and kinetics simulations for WASP-15b's entire atmosphere and its terminator region (separately for the morning and evening terminators, i.e. exactly 90°E and 270°E, respectively, without averaging over the opening angle). The data were averaged over the last 200 simulation days.

APPENDIX G: ADDITIONAL DETAILS REGARDING PHOTOCHEMICAL MODELS

G1 Terminator pressure–temperature profiles, K_{zz} profile, and limb separated transmission spectra

The pressure–temperature profiles at the east and west limbs from the equilibrium UM GCM used for the photochemical modelling are shown in Fig. G1 where we isothermally extend the atmospheric structure to high pressures where photochemistry is the most active. These profiles were averaged over ±20° of each terminator. The K_{zz} profile used in our modelling is also shown in Fig. G1.

In the main text, we show a limb-averaged transmission spectrum for WASP-15b. In Fig. G2, we show the transmission spectra separated for the east/west limbs for our best-fitting 80× solar metallicity case. The SO_2 feature is visible on both limbs with an enhanced amplitude on the cooler west limb as was seen in Tsai et al. (2023).

G2 Molecular line lists used for PICASO opacities

The molecular line lists used to create the opacities in the PICASO radiative transfer modelling are given in Table G1.

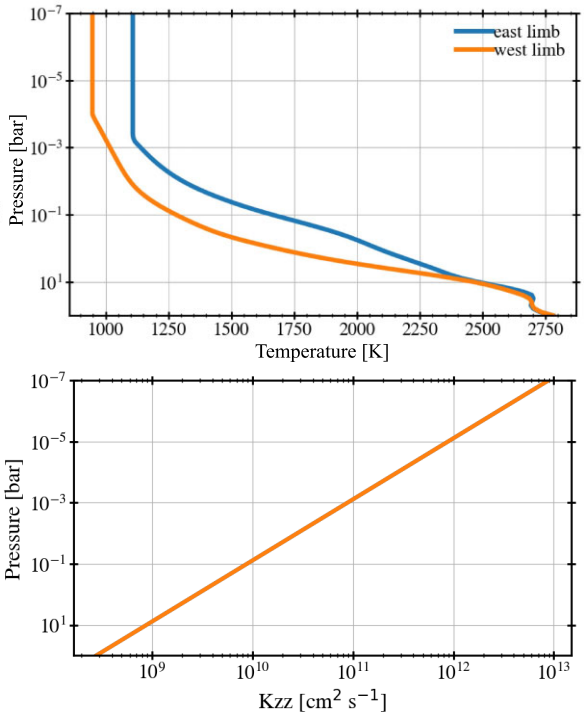

Figure G1. Top: the pressure–temperature profiles at the east and west terminators as calculated from the equilibrium UM GCM, Bottom: the K_{zz} profile used in the photochemical models.

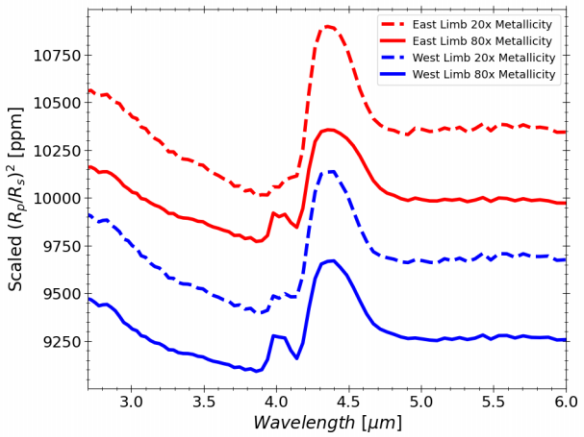

Figure G2. The limb separated transmission spectra based on the photochemical models for WASP-15b for both the 20× and 80× solar models.

Table G1. Line lists used to make PICASO opacities.

Species	Reference
CO_2	Huang et al. (2014)
CH_4	Yurchenko et al. (2013); Yurchenko & Tennyson (2014)
CO	Rothman et al. (2010); Li et al. (2015); Gordon et al. (2017)
H_2	Gordon et al. (2017)
H_2O	Polyansky et al. (2018)
H_2S	Azzam et al. (2016)
H_2–H_2	Lenzuni, Chernoff & Salpeter (1991); Saumon et al. (2012)
H_2–He	Saumon et al. (2012)
H_2–H	Saumon et al. (2012)
H_2–CH_4	Saumon et al. (2012)

[1]*Department of Physics, Imperial College London, Prince Consort Road, London SW7 2AZ, UK*
[2]*Max-Planck-Institut für Astronomie, Königstuhl 17, D-69117 Heidelberg, Germany*
[3]*Centre for Exoplanets and Habitability, University of Warwick, Gibbet Hill Road, Coventry CV4 7AL, UK*
[4]*Department of Physics, University of Warwick, Gibbet Hill Road, Coventry CV4 7AL, UK*
[5]*Department of Physics and Astronomy, Faculty of Environment, Science and Economy, University of Exeter, Exeter EX4 4QL, UK*
[6]*Department of Physics, University of Oxford, Denys Wilkinson Building, Keble Road, Oxford OX1 3RH, UK*
[7]*Department of Astronomy & Astrophysics, University of Chicago, Chicago, IL 60637, USA*
[8]*Department of Physics and Astronomy, Johns Hopkins University, Baltimore, MD 21218, USA*
[9]*Instituto de Astrofísica de Canarias, E-38200 La Laguna, Tenerife, Spain*
[10]*Departamento de Astrofísica, Universidad de La Laguna, E-38206 La Laguna, Tenerife, Spain*
[11]*Department of Earth and Planetary Sciences, University of California, Riverside, CA 92521, USA*
[12]*School of Physics, University of Bristol, HH Wills Physics Laboratory, Tyndall Avenue, Bristol BS8 1TL, UK*
[13]*Department of Astronomy, Cornell University, 122 Sciences Drive, Ithaca, NY 14853, USA*
[14]*School of Physics and Astronomy, University of Leeds, Leeds LS2 9JT, UK*
[15]*Space Telescope Science Institute, 3700 San Martin Drive, Baltimore, MD 21218, USA*
[16]*Center for Astrophysics | Harvard & Smithsonian, 60 Garden St, Cambridge, MA 02138, USA*

This paper has been typeset from a TEX/LATEX file prepared by the author.